Flow organization in the near wake of isolated and sheltered two-dimensional bar roughness elements

Ali M. Hamed ⓘ,[*] Christopher T. O'Brien, Adam J. Hall ⓘ, Ryan M. Gallary,
Joshua J. DaRosa, Quinlan L. Goddard, and Bailey R. McAtee
Department of Mechanical Engineering, Union College, Schenectady, New York 12308, USA

Planar particle image velocimetry and volumetric particle tracking velocimetry were used to investigate the flow over isolated and sheltered two-dimensional bar roughness elements immersed within a turbulent boundary layer. Flow measurements were made for bars occupying up to 17% of the boundary layer thickness at a Reynolds number of 68 000, based on the boundary layer thickness and free stream velocity. In addition to an isolated bar case, the flow was investigated over two bars positioned at streamwise spacings of $0.8h_2$, $1.6h_2$, $2.4h_2$, and $4.8h_2$, where h_2 is the height of the downstream bar. By varying the height of the upstream bar h_1, three height ratios $h_1/h_2 = 0.5$, 0.75, and 1 were considered at each spacing. The results highlight the effects of the spacing and height ratio on the mean flow field and turbulence past the downstream bar. Specifically, sheltering by an upstream bar reduces the reattachment length and velocity deficit past the downstream bar. The introduction of an upstream bar with $h_1/h_2 < 1$ lessens the upwash experienced by the two-bar unit and the overall perturbation to the incoming turbulent boundary layer. The Reynolds shear stress past the downstream bar is also reduced, by up to 45% in some cases, due to sheltering. Overall, the flow organization past the downstream bar is influenced by the flow deflection over the two-bar unit, the upstream bar shear layer, and the structure of flow recirculation between the two bars. Moreover, visualizations of the vortical structures past the isolated bar highlight the growth and evolution of coherent spanwise vortices. Sheltering by an upstream bar enhances the three-dimensionality of the vortical structures in the wake of the downstream bar. The effects of the bar(s) on the boundary layer turbulence structure are investigated through two-point correlations and proper orthogonal decomposition, which suggest a weakening of the large-scale flow structures of the incoming flow.

I. INTRODUCTION

Wall-bounded turbulent flows over periodic and isolated two-dimensional (2D) (transverse) rectangular bar roughness elements have been the subject of numerous experimental and numerical studies. The flow over periodic 2D square bars has been investigated in the context of turbulent boundary layers, channel flows with bars on one or both walls, and open channel flows (e.g., Refs. [1–11]). In addition to the Reynolds number and incoming flow conditions, the flow in such setups is highly dependent on the pitch-to-height ratio p/h, where p is the streamwise spacing from the leading edge of a bar to the leading edge of the next bar, and h is the height of the bars [12–14]. For small streamwise spacings ($p/h \lesssim 8$), the flow exhibits d-type behavior, where the separated flow past a bar reattaches onto the consecutive bar (i.e., the recirculation zone occupies

---

[*]Author to whom all correspondence should be addressed: hameda@union.edu

the entire cavity) [12,13]. In contrast, the flow reattaches to the wall before approaching the next bar for large streamwise spacings ($p/h \gtrsim 8$), exhibiting k-type behavior [12,13]. The ratio of the bars' height to the boundary layer thickness h/δ, or, alternatively, the ratio of the bars' height to the channel's half-height or pipe radius, is a key parameter in the context of outer-layer similarity. Multiple studies noted roughness effects far above the wall (i.e., lack of outer-layer similarity) for periodic bars exhibiting k-type behavior [4,7,15–17]. These studies included bar heights below the $h/\delta \lesssim 2.5\%$ condition suggested by Jimenez [18] for outer-layer similarity (e.g., $h/\delta = 0.62\%$ in Ref. [17]). However, evidence from Krogstad and Efros [19] and Choi *et al.* [10] supports the presence of outer-layer similarity over periodic 2D bars at high Reynolds number and low h/δ; the reader is referred to reviews by Flack and Schultz [20] and Chung *et al.* [21] for further discussion on outer-layer similarity, including over 2D roughness.

In contrast to periodic roughness, an isolated 2D rectangular bar roughness element (obstacle or protrusion) represents a localized perturbation to the incoming smooth-wall boundary layer. The current work focuses on the flow organization in the near wake of such isolated bars and the effects of introducing an additional upstream bar in close proximity. The flow over an isolated 2D rectangular bar is dependent on the Reynolds number, incoming flow conditions, and h/δ. Additionally, Van der Kindere and Ganapathisubramani [22] and Chalmers, Fang, and Tachie [23] highlighted the importance of the streamwise aspect ratio w/h in setting the flow field past isolated rectangular bars; here, w is the streamwise length of the bar. The flow is complicated by separation upstream, above, and downstream of the bar (i.e., the bar can be viewed as a combination of a forward-facing step and a backward-facing step). The likelihood of flow reattachment on the top surface increases with w/h; therefore, the reattachment length and turbulence levels downstream of a bar are significantly larger for low w/h, where reattachment is not achieved on the top surface [22,23]. The flow statistics past isolated square bars with various h/δ have been well documented, including under pressure gradients (e.g., Refs. [24–30]). A separated shear layer develops past the isolated bar, resulting in enhanced turbulence levels that decay in the far wake. Ding and Smits [31] studied turbulent pipe flow past a square bar with $h/R = 0.04$, 0.1, and 0.2, where R is the pipe radius. They divided the flow recovery into three stages: (i) shear layer development, (ii) turbulence redistribution and decay, and (iii) oscillatory and long-lasting recovery. The first stage is characterized by power-law growth in the Reynolds shear stress, extending to the reattachment location X_r, which is dependent on h/R. Another characteristic of the first stage is the confinement of the peak Reynolds shear stress near the top of the bar until $\sim 10h$ downstream. The second stage is marked by power-law decay of the wake turbulence and a vertical redistribution (spreading) of the Reynolds shear stress toward the pipe center. The second stage extends to the streamwise location X_c where the region of high Reynolds shear stress ceases spreading (i.e., the vertical location of the Reynolds shear stress peak no longer increases); the extent of X_c is dependent on h/R. Finally, the flow slowly returns to its unperturbed state with a nonmonotonic recovery in the third stage, which was shown to extend ~ 500–$1000h$.

Numerous studies have explored the effects of isolated 2D bars on the turbulence structure of the incoming boundary layer. For example, multiple studies utilized proper orthogonal decomposition (POD) to gain insight into bar-induced changes in the energy distribution across the flow scales of the incoming flow [22,32–37]. The POD analysis of flow over bars occupying less than 1/3 δ indicates changes in the structure of the low-order POD modes, which are more energetic and typically exhibit a larger scale relative to higher-order modes [32,34,35]. Such changes in low-order POD modes are likely indicative of perturbations to the large-scale motions characteristic of wall-bounded turbulent flows, possibly through the generation of new large-scale structures in the bar wake. Utilizing high-speed wall-pressure and velocity point measurements, Liu, Ke, and Sung [38] investigated the unsteady flow behavior in the near wake of a 2D square bar with $h/\delta \simeq 1.3$. As often observed in backward-facing step flows (e.g., Refs. [39–43]), they suggested the presence of flapping motion in the shear layer separated at the bar leading edge, in addition to the shedding of coherent large-scale vortical structures. The separated shear layer flapping is accompanied by periodic shrinkage and enlargement of the separation bubble [38]. Numerical simulations over

2D bars subjected to uniform flows or thin boundary layers ($h/\delta \gtrsim 1$) have provided insight into the large-scale vortical structures [44–47]. These simulations suggest the formation of coherent spanwise vortical structures due to the roll-up of the shear layer; these structures grow as they advect downstream and become 3D. Details of the unsteady flow behavior and vortical structures past isolated 2D bars immersed within the lower portion of a turbulent boundary layer are lacking in the literature. In such configurations, the bars are subjected to the relatively high shear and turbulence associated with the incoming boundary layer, which likely affect the large-scale vortical structures and their coherence.

In addition to studies on the flow over periodic wall-mounted 2D bars and those on the flow over isolated wall-mounted 2D bars, a few studies have considered the flow interactions between the wakes of two identical wall-mounted 2D bars in close proximity [48–52]. In such setups, the upstream bar shelters the downstream bar from the incoming flow, resulting in drag reduction for the downstream bar relative to an unsheltered isolated one. These studies highlight the sheltering-induced change in the reattachment length past sheltered 2D bars; however, they considered bars occupying a large portion of the boundary layer thickness or channel half-height ($h/\delta \gtrsim 1$). Goswami and Hemmati [53] utilized Reynolds-averaged Navier-Stokes (RANS) simulations to investigate bars with $h/R = 0.1$ and 0.2 in close proximity; they highlighted the limitations of RANS models in correctly capturing flows with high-pressure gradients and recirculation. Studies have also focused on the flow between two 2D bars as a model for street canyons (e.g., Refs. [54–56]). It is worth noting that multiple studies have explored the interactions between the wakes of two tandem roughness elements with various 3D geometries positioned in close proximity (e.g., Refs. [57–63]). Understanding the interactions between the wakes of two roughness elements in close proximity can aid in unraveling the flow physics at the roughness-element scale within the roughness sublayer over irregular multielement rough surfaces [64]. Similarly, the wake interactions between two 2D bars in close proximity may inform the wake interactions among periodic 2D bars, providing insight into the flow dynamics within the roughness sublayer. An understanding of wake interactions can enable a framework where the two-element unit is a building block in low-order models of flow over multiscale distributed roughness (such as the models in Refs. [65–67]).

Building on previous studies of flow over isolated 2D bars, we experimentally study the flow over two identical and nonidentical 2D rectangular bars arranged in close proximity and immersed in a turbulent boundary layer. By varying the streamwise spacing and the height of the upstream bar, we investigate the effects of sheltering on the flow statistics and turbulence structure past the downstream bar and on the turbulent boundary layer perturbation. The results expand on studies of flow over isolated bars and address a gap in the literature on the effects of sheltering on the wake of 2D bars immersed within the lower portion of the boundary layer and subjected to relatively high shear and turbulence levels. The experimental setup is described in Sec. II, the results are reported and discussed in Sec. III, and the conclusions are presented in Sec. IV.

II. EXPERIMENTAL SETUP

The flow over isolated and sheltered 2D rectangular bar roughness elements (obstacles) was experimentally investigated using particle image velocimetry (PIV) in a recirculating, closed water channel. The Engineering Laboratory Design (ELD) water channel has a $0.2 \times 0.2 \times 2$ m^3 test section preceded by a 6:1 area ratio contraction and a flow conditioning module; the reader is referred to Hamed, Peterlein, and Randle [60] for additional details on the channel, which has been previously used to study turbulent boundary layers [11,60,62] and confined shear layers [68]. Twelve arrangements of two bars positioned in close proximity were considered to investigate the effects of sheltering by varying the height ratio h_1/h_2 and the streamwise spacing l/h_2. Here, h_1 and h_2 are the heights of the upstream and downstream bars, respectively, and l is the center-to-center streamwise distance between the two bars. The bars were machined from acrylic stock at the Union College engineering machine shop. All of the bars were carefully aligned in transverse, extended across the entire span of the channel, and had a streamwise length $w = 4.8$ mm $= 0.07\delta_0$, where δ_0
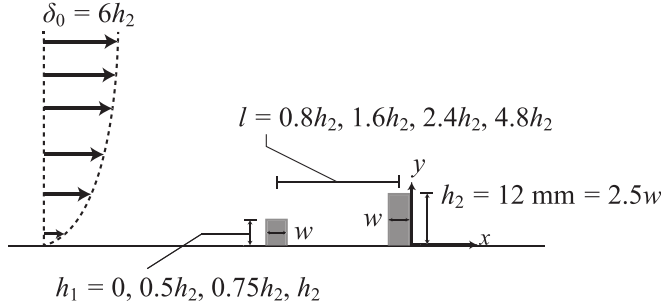
FIG. 1. Schematic of the experimental setup illustrating the configuration of the bars.

is the incoming unperturbed boundary layer thickness at the downstream bar location. The width of the bars was chosen in accordance with the results from Van der Kindere and Ganapathisubramani [22] and Chalmers, Fang, and Tachie [23] to achieve $w/h_1 < 1$ for all upstream bars, evading flow reattachment above the upstream bars. The height of the downstream bar was held constant in all cases at $h_2 = 12$ mm $= 0.17\delta_0$; this height was chosen such that the bar is immersed in the lower portion of the incoming boundary layer, but it is large enough to capture the wake flow in great detail. The height of the upstream bar was varied such that $h_1/h_2 = 0.5$, 0.75, and 1. For each height ratio, the two bars were positioned at streamwise spacings $l/h_2 = 0.8$, 1.6, 2.4, and 4.8 ($l/w = 2$, 4, 6, and 12). These spacings result in a cavity fully occupied by flow recirculation, and, therefore, more pronounced sheltering effects. An additional case with only the downstream bar was considered as a baseline; the configurations are illustrated in Fig. 1. x, y, and z denote the streamwise, wall-normal, and spanwise coordinates, and the origin of the x-coordinate is set at the trailing edge of the downstream bar, which was placed at the same position in all cases ($\sim$1.4 m from the test section inlet).

At the downstream bar location ($x = 0$), the incoming boundary layer has a thickness $\delta_0/h_2 = 6$. This thickness was achieved through five 2D trips positioned following the inlet such that each trip was placed more than 200 trip-element heights upstream of the downstream bar. The locations of the trips and flow conditions were held constant across the 13 cases (isolated bar and 12 two-bar arrangements), allowing for meaningful comparisons. The incoming unperturbed (i.e., with trips but without bars) turbulent boundary layer statistics at $x = 0$ are shown in Fig. 2, including the time-averaged streamwise velocity U/U_0, the streamwise turbulence intensity σ_u/U_0, and the Reynolds shear stress $-\langle u'v' \rangle/u_\tau^2$. Here, $U_0 = 0.954$ m/s is the free stream velocity; u_τ is the friction velocity; $\langle \cdot \rangle$ denotes temporal averaging such that $U = \langle u \rangle$; u is the instantaneous streamwise velocity; and primes indicate temporal fluctuations from time-averaged quantities (e.g., $u' = u - U$). Determining u_τ without direct measurements of the wall shear stress is challenging; the reader is referred to Wei, Schmidt, and McMurtry [69], Smits, McKeon, and Marusic [70], Marusic *et al.* [71], and Djenidi, Talluru, and Antonia [72] for a discussion of the challenge in obtaining u_τ from the velocity profile, especially at moderate Reynolds number (here, $Re_\tau = u_\tau \delta_0/\nu = 2,500$, where ν is the kinematic viscosity). However, an estimate of u_τ can be obtained from the maximum or plateau of the total stress profile or the Reynolds shear stress profile (e.g., as in Refs. [16,73–75]). Here, $u_\tau = 0.035$ m/s is estimated as the square root of the maximum Reynolds shear stress. u_τ is also estimated by fitting the velocity profile to the log law; the resulting u_τ agrees with the value reported above (8% difference, with a von Kármán's constant $\kappa = 0.41$ and an additive constant $B = 5.4$). In Fig. 2(c), the maximum Reynolds shear stress of 1 is an artifact of the method chosen to estimate u_τ. At $x = 0$, the unperturbed boundary layer has a displacement thickness $\delta^*/\delta_0 = 0.119$ and a momentum thickness $\theta/\delta_0 = 0.088$. Although based on integral quantities, the shape factor δ^*/θ provides a quantitative evaluation of the time-averaged streamwise velocity profile without the need for u_τ [76]. The shape factor found here ($\delta^*/\theta = 1.35$) is similar to the shape
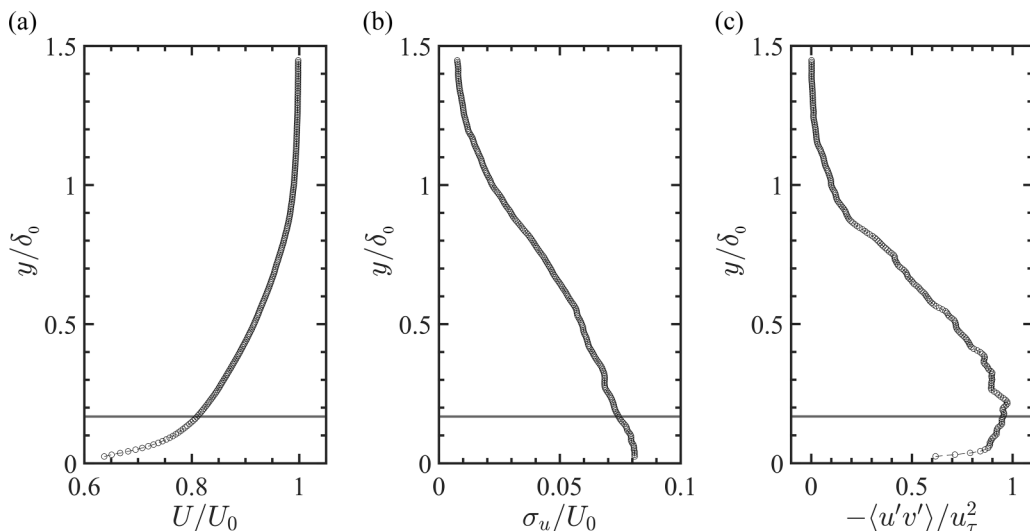
FIG. 2. Statistics of the unperturbed (with trips but without bars) incoming turbulent boundary layer at $x = 0$: (a) the time-averaged streamwise velocity U/U_0, (b) the streamwise turbulence intensity σ_u/U_0, and (c) the Reynolds shear stress $-\langle u'v' \rangle/u_\tau^2$. The horizontal line at $y/\delta_0 = 0.17$ indicates the top of the downstream bar.

factor values reported in the literature for zero pressure gradient boundary layers at similar $\mathrm{Re}_\theta = U_0\theta/\nu = 6000$ (see Fig. 13 in Ref. [77] for the shape factor as a function of Re_θ based on multiple studies). Planar PIV measurements were made in the central streamwise-wall-normal (x-y) plane at Reynolds number $\mathrm{Re} = U_0\delta_0/\nu = 68\,000$. Within the measurement region $-6.8 \leqslant x/h_2 \leqslant 14.7$ ($-1.1 \leqslant x/\delta_0 \leqslant 2.5$), the unperturbed boundary layer has a pressure gradient near zero as evidenced by a negligible change in U_0 ($<0.7\%$), and it approaches a developed stage with $<2\%$ change in the local boundary layer thickness. The boundary layers on the three remaining channel walls are untripped, resulting in thinner boundary layers with thickness $\sim 2.5h_2$ at the measurement region. Therefore, the $11.7h_2$ central region of the bars is outside of the boundary layers developed on the side walls. In the wall-normal direction, the edge of the unperturbed boundary layer is $7.2h_2$ away from the edge of the boundary layer on the opposite wall. As such, the flow within the measurement region is overall free from the boundary layers formed on the other channel walls.

Flow measurements in the central streamwise-wall-normal (x-y) plane were made using a TSI 2D PIV system consisting of a 16-MP CCD camera and a 200 mJ/pulse double-pulsed Nd:YAG laser. Hollow glass spheres with 10 μm average diameter were used as seeding particles and were illuminated by a 1-mm-thick laser sheet. Flow measurements were made in two fields of view (FOVs): a large FOV ($x \times y = 258 \times 179$ mm^2 $= 21.5h_2 \times 14.9h_2 = 3.6\delta_0 \times 2.5\delta_0$) and a small FOV ($x \times y = 114 \times 80$ mm^2 $= 9.5h_2 \times 6.7h_2 = 1.6\delta_0 \times 1.1\delta_0$). The large FOV provides the flow details in the near wake of the downstream bar, while the small FOV illustrates the flow between the two bars. For both FOVs, image pairs were collected at a frequency of 1 Hz; the 1 s interval between image pairs is significantly larger than the integral timescale of the flow, which was roughly estimated based on the free stream velocity and boundary layer thickness. The image pairs were interrogated in Insight 4G (TSI) using a multipass scheme. A 16×16 pixel final interrogation window was chosen with 50% overlap, resulting in a final vector grid spacing of $\Delta x = \Delta y = 0.44$ mm $= 0.037h_2$ and $\Delta x = \Delta y = 0.20$ mm $= 0.017h_2$ for the large and small FOVs, respectively. To minimize peak-locking bias error, the average particle image diameter was above the two-pixel limit, as recommended by Christensen [78]. Random errors in determining particle displacement have been approximated to 5% of the particle image diameter [79]; this amounts to $\sim 1\% U_0$ for both FOVs. For the large FOV, 4000 statistically independent velocity fields were

acquired for each of the 13 cases to quantitatively describe the flow in the wake of the downstream bar. For the small FOV, 1000 statistically independent velocity fields were acquired for each case to visualize the flow between the two bars. Overall, the flow conditions, PIV setup, and PIV image-pair interrogation scheme were consistent across the 13 cases, allowing for meaningful comparisons.

To gain further insight into the flow organization in the near wake of the downstream bar, volumetric three-component flow measurements were made for four cases: (i) the isolated bar; (ii) $l/h_2 = 0.8$, $h_1/h_2 = 0.75$; (iii) $l/h_2 = 1.6$, $h_1/h_2 = 0.75$; and (iv) $l/h_2 = 4.8$, $h_1/h_2 = 0.75$. The measurements were made using a high-speed 3D particle tracking velocimetry (PTV) system (V3V-Flex) from TSI. The system consists of four Phantom VEO 440 4-MP high-speed cameras and a Northrop Grumman 40 mJ/pulse high-speed double-pulsed laser. The four cameras were positioned in-line with an $\sim30°$ angle between the two outer cameras, resulting in four distinct perspectives of a volume of interest (VOI) with a size $x \times y \times z = 96 \times 52 \times 72$ mm$^3 = 8.0h_2 \times 4.3h_2 \times 6.0h_2 = 1.3\delta_0 \times 0.7\delta_0 \times 1.0\delta_0$. Each camera was equipped with Scheimpflug adapter and a 135 mm lens. Silver-coated hollow glass spheres with a 50 μm average diameter were used as seeding particles and were illuminated within the VOI by the high-speed Nd:YLF laser. Image pairs were acquired at 250 Hz and later processed using Insight V3V software (TSI). Specifically, a three-step scheme was applied to each image pair to determine the three-component velocity within the VOI. First, particles were identified in each of the eight images (four cameras at two consecutive times). Second, the identified particles were triangulated into 3D space based on a multiplane calibration and matched across the four cameras. Third, the particles were tracked across the two consecutive times, and the resulting randomly spaced velocity vectors were interpolated onto a rectangular grid. The reader is referred to Refs. [80,81] for additional details on the particle identification, reconstruction, matching, and tracking scheme. Relative to previous V3V systems (such as the one used in Ref. [82]), the V3V-Flex system allows for flexibility in positioning the cameras and utilizes a recursive particle identification and matching algorithm [steps (i) and (ii) of the three-step processing scheme outlined above]; this recursive algorithm is known as the dense particle identification and reconstruction (DPIR) algorithm. To ensure sufficient flow fields for analysis, 13 500 volumetric three-component velocity fields were obtained for each of the four aforementioned cases. On average, an image pair resulted in 24 700 independent randomly spaced velocity vectors. These vectors were interpolated onto a rectangular grid with a $6 \times 6 \times 6$ mm$^3 = 0.5h_2 \times 0.5h_2 \times 0.5h_2$ voxel size at 50% overlap, resulting in a final vector grid spacing $\Delta x = \Delta y = \Delta z = 3$ mm $= 0.25h_2$. Global and local vector validation was used to ensure the quality of the obtained velocity fields. The velocity uncertainty in these volumetric measurements stems from errors in particle identification and triangulation; the uncertainty is estimated to be $\sim1.5\%U_0$ for u and w and $\sim5.6\%U_0$ for v.

III. RESULTS AND DISCUSSION

A. The mean flow field

The mean flow field over the isolated bar is illustrated in Fig. 3 through contours of the time-averaged streamwise and wall-normal velocities U/U_0 and V/U_0, respectively. Streamlines and a white contour at $U/U_0 = 0$ are added to Fig. 3(a) to aid in visualizing flow recirculation. In this and subsequent contour plots, regions without color contours (white space) indicate locations where the flow velocity was not obtained due to shadows or exterior optical obstructions. Here and in subsequent results, h_2 is used for normalization to highlight the flow features in the near wake and to facilitate comparisons with previous studies (e.g., Refs. [22,23,31]). As expected, the flow decelerates upstream of the bar and deflects upward, resulting in a region of intense upwash with V reaching up to $\sim45\%U_0$. As seen in Fig. 3, the bar-induced deceleration extends to at least $x/h_2 = -6$, and the upwash extends beyond $y/h_2 = 6$ ($y/\delta_0 = 1$). A relatively weak downwash region, with V as low as $-8\%U_0$, develops over the downstream part of the large recirculation zone, which dominates the near wake. Small recirculation zones form at the bar-wall junction on both the upstream and downstream sides; the recirculation zone on the upstream side was confirmed using
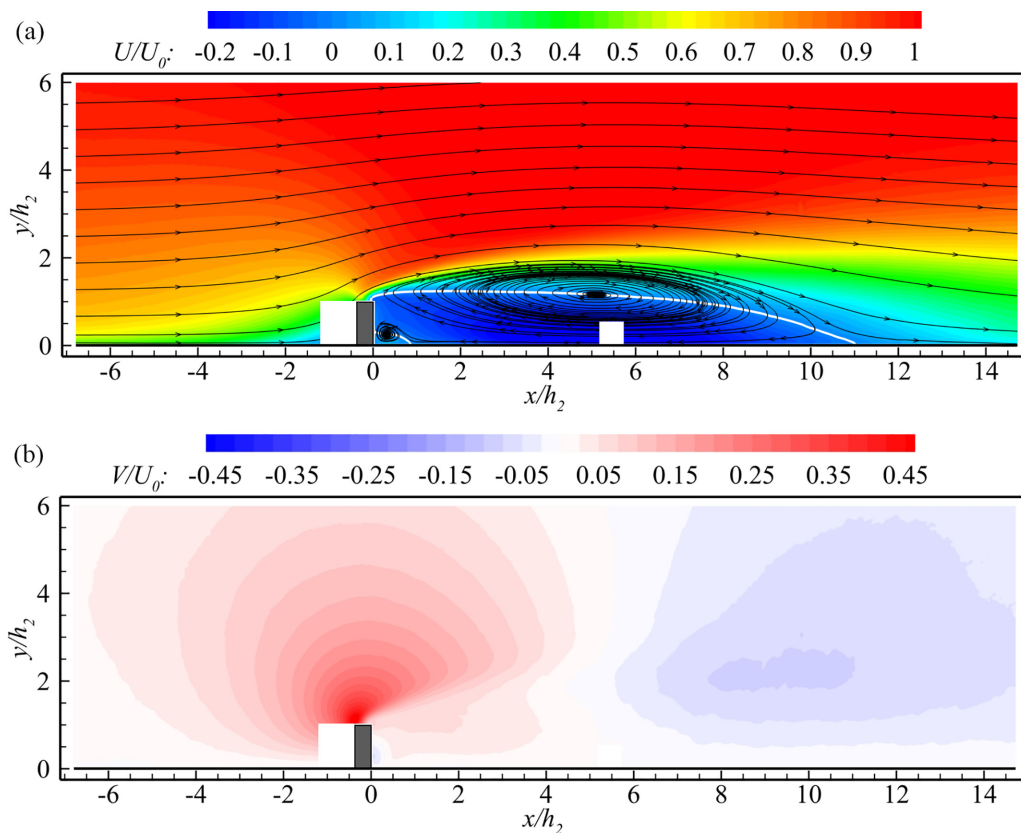
FIG. 3. Mean flow field over the isolated bar: (a) time-averaged streamwise velocity U/U_0 and (b) time-averaged wall-normal velocity V/U_0. Streamlines and a white contour at $U/U_0 = 0$ are added to (a) to visualize flow recirculation. Here and in subsequent figures, regions without color contours indicate locations where the flow velocity was not obtained due to shadows or exterior optical obstructions, and the gray rectangle(s) represent the bar(s).

the small FOV PIV measurements. As evidenced by the volumetric flow measurements, the planar PIV results presented here are consistent with other spanwise locations; as expected, the mean flow is 2D within the central region of the bar(s) away from the side walls. The flow field presented in Fig. 3 and the reattachment length $X_r/h_2 = 11.0$, determined at the intersection of the $U/U_0 = 0$ contour and the wall, are consistent with previous studies on isolated bars [22,23,31,35].

For the two-bar cases, flow recirculation occupies the entire cavity between the two bars as discussed below, and the flow field exhibits features similar to those seen in Fig. 3. Specifically, the flow field is characterized by an intense upwash region at the upstream bar, flow recirculation between the two bars and behind the downstream bar, and an extended downwash region. While the large-scale flow features are similar to those over the isolated bar, significant changes in the reattachment length and upwash/downwash distribution occur as a result of sheltering by an upstream bar. As an example, Fig. 4 shows the flow field for the $l/h_2 = 0.8$, $h_1/h_2 = 0.75$ case; here, the reattachment length is reduced from $X_r/h_2 = 11.0$ for the isolated bar case to $X_r/h_2 = 6.7$, and the upwash is reduced in both magnitude and extent.

As shown in Fig. 5, the reattachment length X_r/h_2 is highly dependent on both the streamwise spacing l/h_2 and the height ratio h_1/h_2. For a given h_1/h_2, the reattachment length decreases as l/h_2 increases; a similar trend has been noted for identical bars ($h_1/h_2 = 1$) with $h_2 > \delta_0$ [49,52]. In particular, Liou, Chang, and Hwang [49] investigated flow reattachment past identical bars with
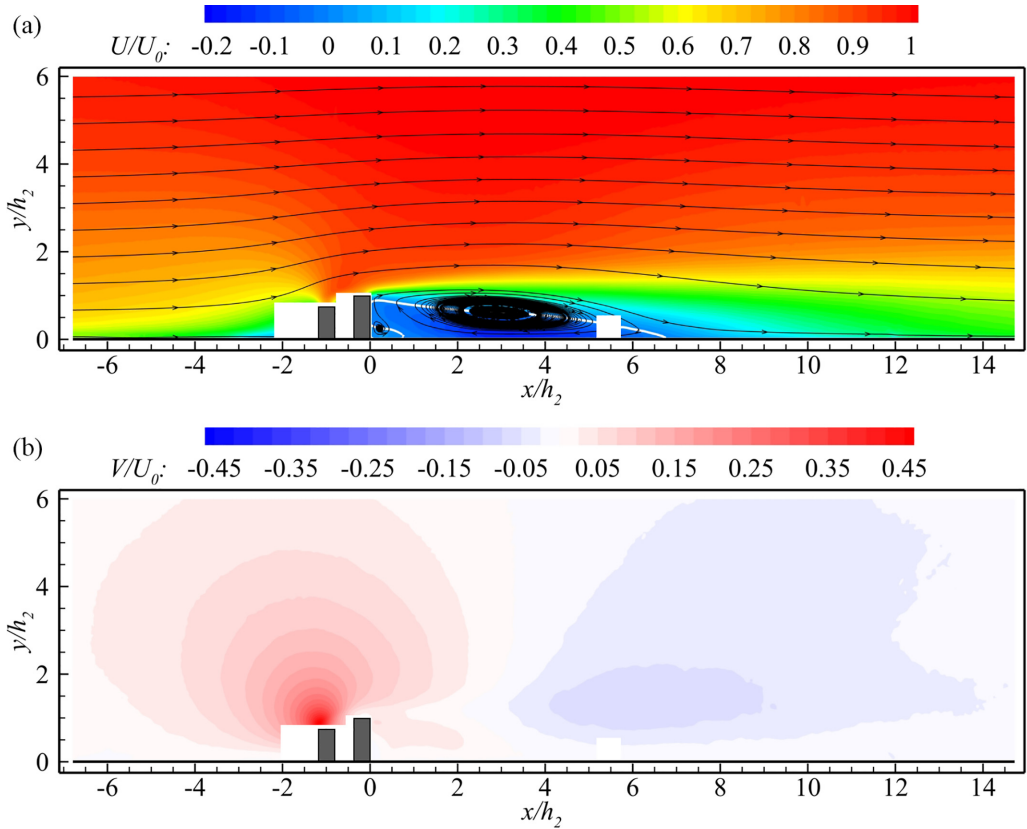
FIG. 4. Mean flow field for the $l/h_2 = 0.8$, $h_1/h_2 = 0.75$ case: (a) time-averaged streamwise velocity U/U_0 and (b) time-averaged wall-normal velocity V/U_0. Streamlines and a white contour at $U/U_0 = 0$ are added to (a) to visualize flow recirculation.

$l/h_2 = 1 - 100$; they noted a decreasing X_r/h_2 for $l/h_2 < 5$, a near constant X_r/h_2 for $5 < l/h_2 < 20$, an increasing X_r/h_2 for $20 < l/h_2 < 80$, and a constant X_r/h_2 for $l/h_2 > 80$. They suggested that the decrease in X_r/h_2 for $l/h_2 < 5$ is related to the decrease in the pressure on the top surface of the downstream bar, resulting in increased suction of the separated shear layer stemming from the upstream bar. Additionally, the turbulence and entrainment of higher momentum outer flow associated with the upstream bar shear layer weakens the flow recirculation past the downstream bar. The role of the turbulence associated with the upstream bar wake in enhancing mixing and reducing X_r/h_2 is supported by the results presented here (e.g., X_r/h_2 is reduced for all two-bar cases relative to the isolated bar case). The role of upstream turbulence and mixing in weakening flow recirculation is also supported in the literature, motivating flow recirculation control strategies such as vortex generators to enhance mixing and momentum transfer (see a key review on vortex generators by Lin [83] and studies by Park *et al.* [84] and Ma, Geisler, and Schröder [85] on using vortex generators to control flow recirculation past backward-facing steps). At a given l/h_2, significant variations are noted in X_r/h_2 due to h_1/h_2 (Fig. 5). For example, the introduction of an upstream bar at $l/h_2 = 0.8$ shortens the reattachment length relative to the isolated bar case by $0.5h_2$, $4.3h_2$, and $2.0h_2$ for $h_1/h_2 = 0.5$, 0.75, and 1, respectively. For $l/h_2 = 1.6$, 2.4, and 4.8, the $h_1/h_2 = 1$ cases have the largest X_r/h_2, followed by the $h_1/h_2 = 0.5$ cases and then by the $h_1/h_2 = 0.75$ cases. Relative to the $h_1/h_2 = 1$ cases, the reduction in X_r/h_2 for the $h_1/h_2 = 0.5$ and $h_1/h_2 = 0.75$ cases is likely related to a more gradual flow deflection and reduced upwash for these cases, as discussed below. At $l/h_2 = 0.8$, the $h_1/h_2 = 0.5$ case has a larger X_r/h_2 compared to the $h_1/h_2 = 1$ case; this is likely
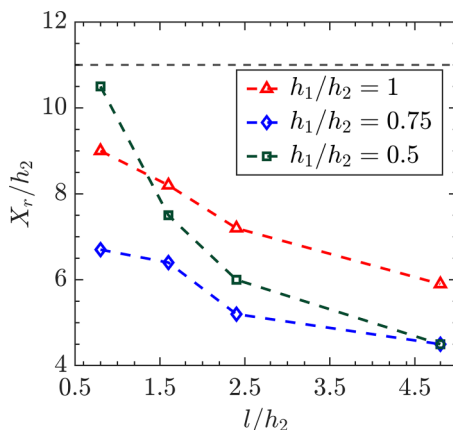
FIG. 5. The reattachment length X_r/h_2 as a function of the streamwise spacing l/h_2 and the height ratio h_1/h_2. The dashed line at $X_r/h_2 = 11.0$ indicates the reattachment length past the isolated bar.

due to a combination of a less effective reduction in upwash and a shear layer at h_1 that does not spread to h_2 due to the low l/h_2. Across all l/h_2, the $h_1/h_2 = 0.75$ cases exhibit the lowest X_r/h_2. The remarkable reduction in X_r/h_2 for the $h_1/h_2 = 0.75$ cases is likely due to a combination of reduced upwash, a shear layer at h_1 that spreads to h_2, and a favorable flow recirculation pattern within the cavity between the two bars. The flow pattern between the two bars is discussed further below.

The h_1/h_2-induced variations in V/U_0 over the two-bar unit are illustrated in Fig. 6 through streamwise profiles at $y/h_2 = 2$. For the isolated bar case, V/U_0 increases until it peaks at roughly the center of the bar; V/U_0 then decreases to a minimum at $x/h_2 \simeq 8$ (i.e., upstream of reattachment) before a gradual recovery extending past $x/h_2 = 15$. The overall V/U_0 trend is similar for the other cases, but the streamwise location and magnitude of the maximum/minimum vary with l/h_2 and h_1/h_2. The presence of a short upstream bar ($h_1/h_2 < 1$) results in a more gradual flow deflection and a less intense upwash region. At $l/h_2 = 1.6$ [Fig. 6(b)], for example, the maximum wall-normal velocity at $y/h_2 = 2$ decreases from $26\%U_0$ for the isolated bar and the $h_1/h_2 = 1$ cases to $16\%U_0$ and $13\%U_0$ for the $h_1/h_2 = 0.75$ and $h_1/h_2 = 0.5$ cases, respectively. Interestingly, V/U_0 for the $h_1/h_2 = 0.5$ cases is below that of the $h_1/h_2 = 0.75$ cases for all streamwise spacings except for $l/h_2 = 0.8$ (Fig. 6). As such, an upstream bar with $h_1/h_2 = 0.5$ is less effective in reducing the flow deflection and upwash when positioned at a short streamwise distance ($l/h_2 = 0.8$), which likely contributes to the increased X_r/h_2 for this case (Fig. 5). While the presence of a short upstream bar ($h_1/h_2 < 1$) reduces the reattachment length and the maximum V/U_0 for all cases, the reduction is dependent on both l/h_2 and h_1/h_2 (Figs. 5 and 6), suggesting flow control opportunities to reduce drag and boundary layer perturbation in engineering applications utilizing 2D bars. Direct drag measurements are needed to quantify such drag reduction potentials.

The sensitivity of the cavity flow to l/h_2 and h_1/h_2 is illustrated in Figs. 7 and 8 through contours of V/U_0 and streamlines obtained from the small FOV PIV measurements, which were performed specifically to visualize the flow in the cavity. In all two-bar cases, the cavity is fully occupied with flow recirculation; the structure of the cavity flow has important implications for transport in, for example, street canyons (e.g., Refs. [54–56]). Figure 7 highlights the effects of introducing an upstream bar with $h_1/h_2 = 0.75$ at the various l/h_2. For $l/h_2 = 0.8$ [Fig. 7(b)], the cavity is occupied by two recirculation zones of similar size and opposite sense of rotation. For larger l/h_2 [Figs. 7(c)–7(e)], the cavity is occupied by a large recirculation zone, which elongates in the streamwise direction with increasing l/h_2. For the $l/h_2 \geqslant 1.6$ cases [Figs. 7(c)–7(e)], a relatively small recirculation zone forms at each corner of the cavity near the wall. Together, Figs. 7(c) and 8 highlight the effects of h_1/h_2 on the flow structure within the cavity at $l/h_2 = 1.6$. As the height
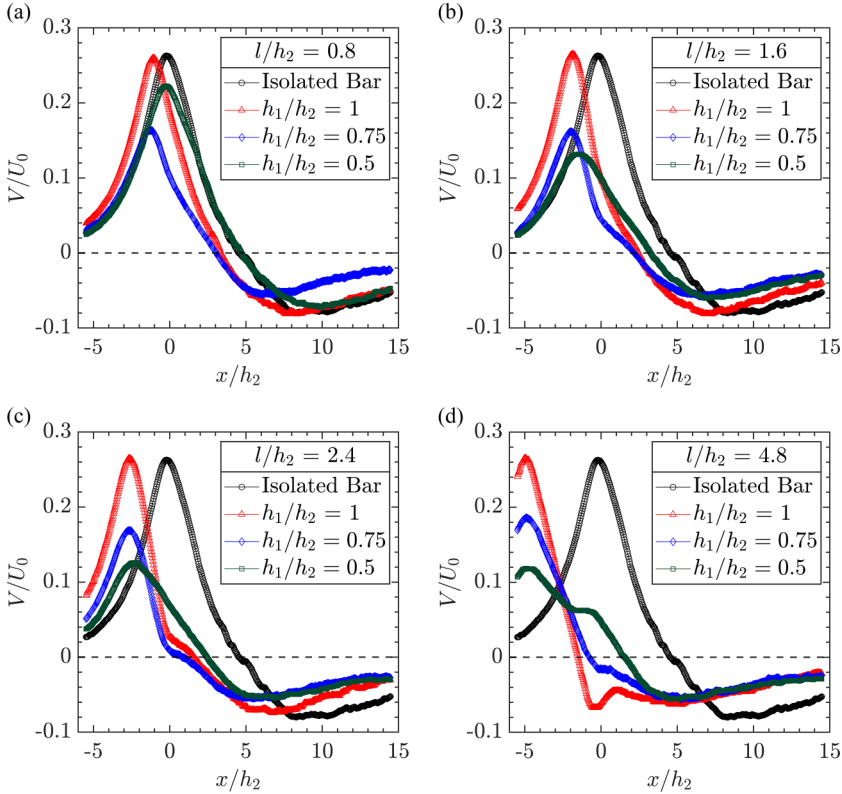
FIG. 6. Streamwise profiles of the time-averaged wall-normal velocity V/U_0 at $y/h_2 = 2$ ($y/\delta_0 = 0.33$): (a) $l/h_2 = 0.8$, (b) $l/h_2 = 1.6$, (c) $l/h_2 = 2.4$, and (d) $l/h_2 = 4.8$. The isolated bar case is shown in all subfigures to aid in comparison.

of the upstream bar increases, the vertical extent of flow recirculation increases, reaching above the downstream bar for the $h_1/h_2 = 1$ case [Fig. 8(b)]. The structure of the flow recirculation within the cavity has critical consequences for flow reattachment and recovery past the downstream bar. For example, the slightly elevated recirculation zone for the $h_1/h_2 = 0.75$ case [Fig. 7(c)] relative to the $h_1/h_2 = 0.5$ case [Fig. 8(a)] results in favorable conditions for flow recovery. Namely, the leading edge of the downstream bar at $y/h_2 = 1$ is subjected to downward flow in the $h_1/h_2 = 0.75$ case [Fig. 7(c)]. This downward flow possibly explains the reduced reattachment length for this case ($X_r/h_2 = 6.4$) relative to the $h_1/h_2 = 0.5$ case ($X_r/h_2 = 7.5$), where the flow deflects upward at the leading edge of the downstream bar [Fig. 8(a)]. For the $h_1/h_2 = 1$ case [Fig. 8(b)], the recirculation zone engulfs the downstream bar, resulting in a relatively lengthy X_r/h_2 for this case ($X_r/h_2 = 8.2$).

Figures 3–8 highlight the effects of sheltering by an upstream bar on the wake of a downstream bar; these effects culminate in a reattachment length X_r/h_2 that is highly sensitive to both l/h_2 and h_1/h_2. The dependency on h_1/h_2 and l/h_2 manifests through multiple mechanisms, including the more gradual upward flow deflection and reduced upwash due to upstream bars with $h_1/h_2 < 1$. While the reduction in upwash is strongly governed by h_1/h_2 (Fig. 6), it is not independent of l/h_2. Another mechanism governing the downstream bar wake is the turbulence and entrainment associated with the shear layer past the upstream bar, which has a significant role in reducing X_r/h_2 [49]. Since the shear layer past the upstream bar develops in the streamwise direction and spreads vertically with a peak near h_1 [31], the position of the downstream bar relative to the upstream bar (i.e., l/h_2) determines the levels of turbulence it will experience. A third mechanism is the structure of the cavity flow, which is highly dependent on l/h_2 and h_1/h_2 (Figs. 7 and 8). The
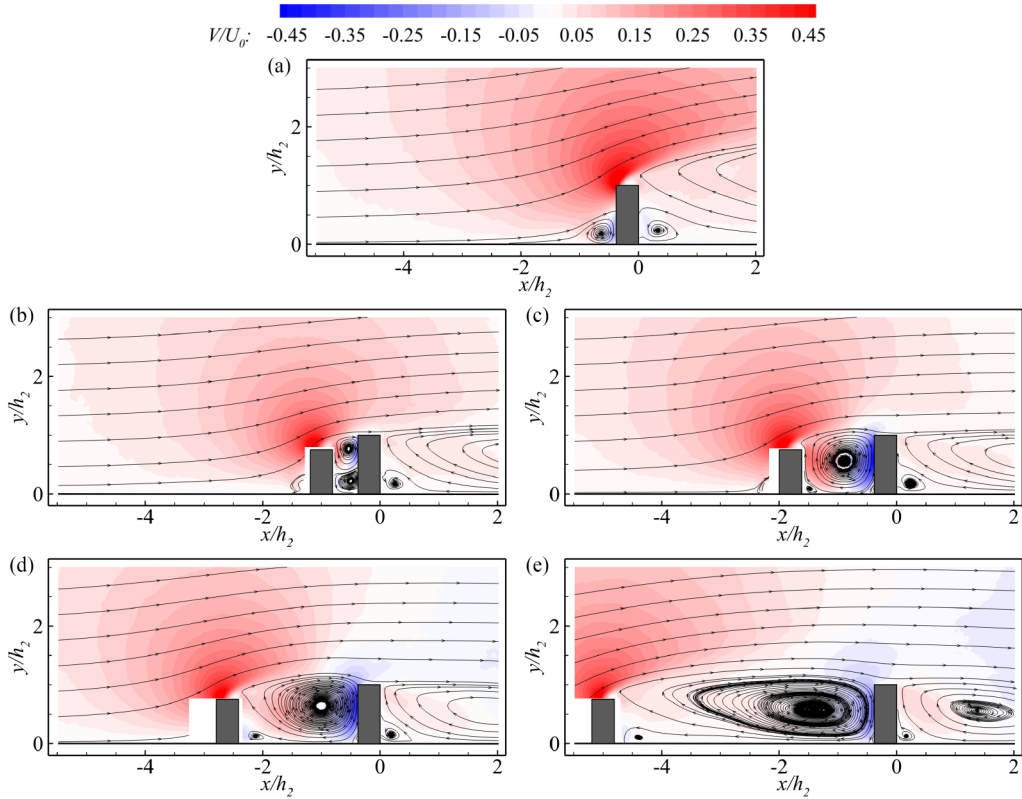
FIG. 7. Streamlines and time-averaged wall-normal velocity V/U_0 contours for (a) the isolated bar case and (b)–(e) the $h_1/h_2 = 0.75$ cases.

structure of the cavity flow determines the conditions at the leading edge of the downstream bar at $y/h_2 = 1$ (i.e., engulfed in a recirculation zone, subjected to downward flow, or subjected to upward flow). Together, these mechanisms govern the reattachment length X_r/h_2 provided in Fig. 5. The combination of these mechanisms appears to favor the $h_1/h_2 = 0.75$ cases, resulting in the lowest X_r/h_2.

To examine the boundary layer perturbation by isolated and sheltered 2D bars, Fig. 9 provides profiles of the velocity deficit $\Delta U/U_0 = (U_{ref} - U)/U_0$ at $x/h_2 = 2$ and 14. Here, U_{ref}/U_0 denotes the incoming velocity profile in the absence of any bars [Fig. 2(a)], and δ_0 is used for normalization to highlight the vertical extent of the perturbation to the boundary layer. As shown in Fig. 9, a
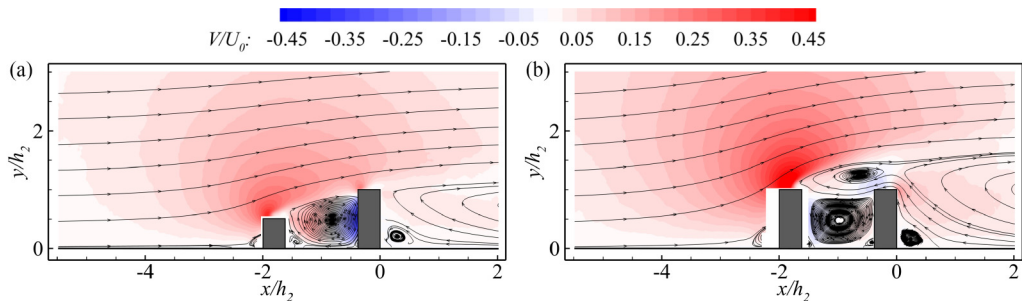
FIG. 8. Streamlines and time-averaged wall-normal velocity V/U_0 contours for (a) the $l/h_2 = 1.6, h_1/h_2 = 0.5$ case and (b) the $l/h_2 = 1.6, h_1/h_2 = 1$ case.
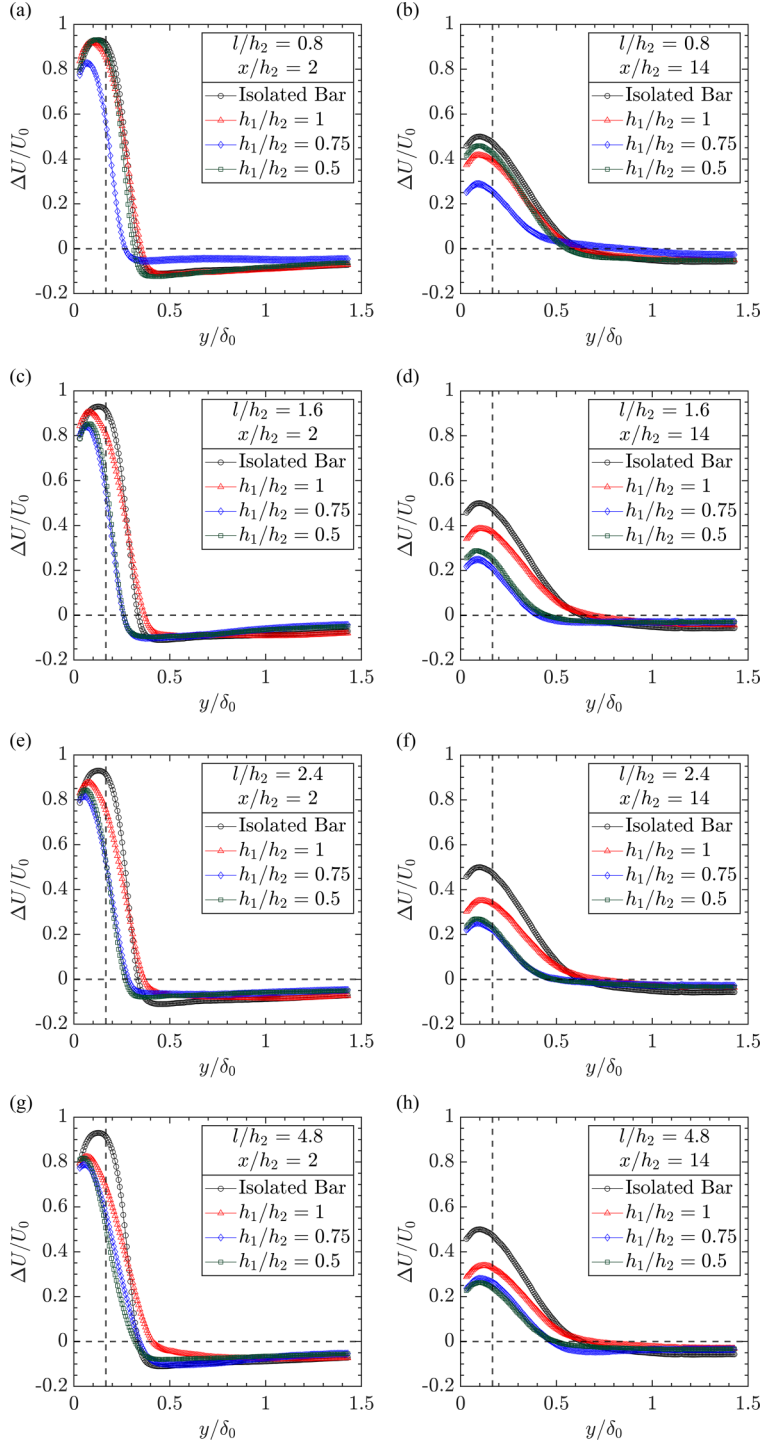
FIG. 9. Wall-normal profiles of the flow deficit relative to the unperturbed boundary layer $\Delta U/U_0$ at $x/h_2 = 2$ (left) and $x/h_2 = 14$ (right): (a) and (b) $l/h_2 = 0.8$, (c) and (d) $l/h_2 = 1.6$, (e) and (f) $l/h_2 = 2.4$, and (g) and (h) $l/h_2 = 4.8$. The vertical dashed line at $y/\delta_0 = 0.17$ indicates the top of the downstream bar. The isolated bar case is shown in all subfigures to aid in comparison.

velocity deficit (positive $\Delta U/U_0$) is observed at heights extending up to $y/\delta_0 = 0.4$ ($y/h_2 = 2.4$) at $x/h_2 = 2$. As the shear layer past the downstream bar grows, the deficit penetrates as high as $y/\delta_0 = 0.8$ ($y/h_2 = 4.8$) at $x/h_2 = 14$. The extent and magnitude of the velocity deficit are dependent on x/h_2, l/h_2, and h_1/h_2. In addition to the flow deficit, flow speedup (negative $\Delta U/U_0$) reaching up to $12\%U_0$ occurs in the upper part of the boundary layer and extends past $y/\delta_0 = 1$. Similarly, the flow speedup is dependent on x/h_2, l/h_2, and h_1/h_2. Both the velocity deficit and speedup persist past $x/h_2 = 14$. Overall, sheltering by an upstream bar reduces the flow deficit past the downstream bar through the reduction of the reattachment length (Fig. 5) and the more gradual flow deflection for the $h_1/h_2 < 1$ cases (Fig. 6). Therefore, sheltering results in a milder perturbation to the incoming boundary layer. In particular, $h_1/h_2 = 0.75$ is very effective in reducing boundary layer perturbation across the considered l/h_2.

B. The turbulence and its structure

Contours of the Reynolds shear stress $-\langle u'v'\rangle/U_0^2$ are shown in Fig. 10 for the isolated bar; $l/h_2 = 0.8$, $h_1/h_2 = 0.75$; and $l/h_2 = 4.8$, $h_1/h_2 = 0.75$ cases. Across these and other cases, elevated $-\langle u'v'\rangle/U_0^2$ levels are associated with the shear layer past the upstream and downstream bars. The in-plane turbulent kinetic energy TKE $= \langle u'^2 + v'^2\rangle/2U_0^2$, not shown for brevity, exhibits a similar spatial distribution to $-\langle u'v'\rangle/U_0^2$. The spanwise Reynolds normal stress $\langle w'^2\rangle/U_0^2$, captured for four cases using the volumetric flow measurements, is similar in magnitude to the wall-normal Reynolds normal stress $\langle v'^2\rangle/U_0^2$. For the isolated bar [Fig. 10(a)], $-\langle u'v'\rangle/U_0^2$ exhibits similar characteristics to those described by Ding and Smits [31] within the first stage of flow recovery: shear layer development. As shown in Fig. 10(a), $-\langle u'v'\rangle/U_0^2$ grows until $x/h_2 \simeq 7.6$ ($x/X_r \simeq 0.7$) and then plateaus. Past the reattachment point ($x/h_2 = 11.0$), $-\langle u'v'\rangle/U_0^2$ begins to decay [Fig. 10(a)], marking the start of the second flow recovery stage: turbulence redistribution and decay. The third stage of flow recovery, oscillatory and long-lasting recovery, is expected further downstream past the end of the measurement region. As shown in Fig. 10, the introduction of an upstream bar alters the $-\langle u'v'\rangle/U_0^2$ distribution; in particular, the maximum $-\langle u'v'\rangle/U_0^2$ is reduced for all two-bar cases relative to the isolated bar case. In some cases, the reduction is significant; for example, the introduction of a bar at $l/h_2 = 0.8$ and $h_1/h_2 = 0.75$ [Fig. 10(b)] results in a 45% reduction in the maximum $-\langle u'v'\rangle/U_0^2$ relative to the isolated bar case. Moreover, the introduction of an upstream bar complicates the first flow recovery stage described by Ding and Smits [31]. The growth in $-\langle u'v'\rangle/U_0^2$ associated with the shear layer past the upstream bar is interrupted by the downstream bar [Figs. 10(b) and 10(c)]. As noted earlier, the turbulence and entrainment of higher momentum outer flow associated with the upstream bar shear layer weaken the flow recirculation past the downstream bar to different degrees determined by h_1 and l/h_2; further investigations are needed to quantify this entrainment and its physical mechanisms. The shear layer past the downstream bar experiences growth in $-\langle u'v'\rangle/U_0^2$ [Figs. 10(b) and 10(c)]; as such, the shear layer development stage for the two-bar unit extends from the upstream bar to the reattachment point past the downstream bar. Due to the interruption by the downstream bar, the first stage is not characterized by continual growth in $-\langle u'v'\rangle/U_0^2$. Near the reattachment point, $-\langle u'v'\rangle/U_0^2$ begins to decay, as expected in the second recovery stage.

The effects of l/h_2 and h_1/h_2 on the Reynolds shear stress $-\langle u'v'\rangle/U_0^2$ and on the incoming flow turbulence are quantitatively investigated in Fig. 11 through profiles of the Reynolds shear stress deficit $\Delta\langle -u'v'\rangle/U_0^2 = \langle -u'v'\rangle_{\text{ref}}/U_0^2 - \langle -u'v'\rangle/U_0^2$. $\langle -u'v'\rangle_{\text{ref}}/U_0^2$ is the incoming Reynolds shear stress profile in the absence of any bars [Fig. 2(c)]. Here, positive $\Delta\langle -u'v'\rangle/U_0^2$ indicates a Reynolds shear stress deficit relative to the unperturbed boundary layer, while a negative $\Delta\langle -u'v'\rangle/U_0^2$ indicates a Reynolds shear stress surplus relative to the unperturbed boundary layer. In Fig. 11, profiles are provided at $x/h_2 = 2$ and 14 to highlight the growth of the shear layer, and δ_0 is used for normalization to highlight the vertical extent of the perturbation to the boundary layer. The minimum $\Delta\langle -u'v'\rangle/U_0^2$ occurs at different streamwise locations for the various cases; therefore, some of the two-bar cases exhibit a more pronounced $\Delta\langle -u'v'\rangle/U_0^2$ value than the isolated bar
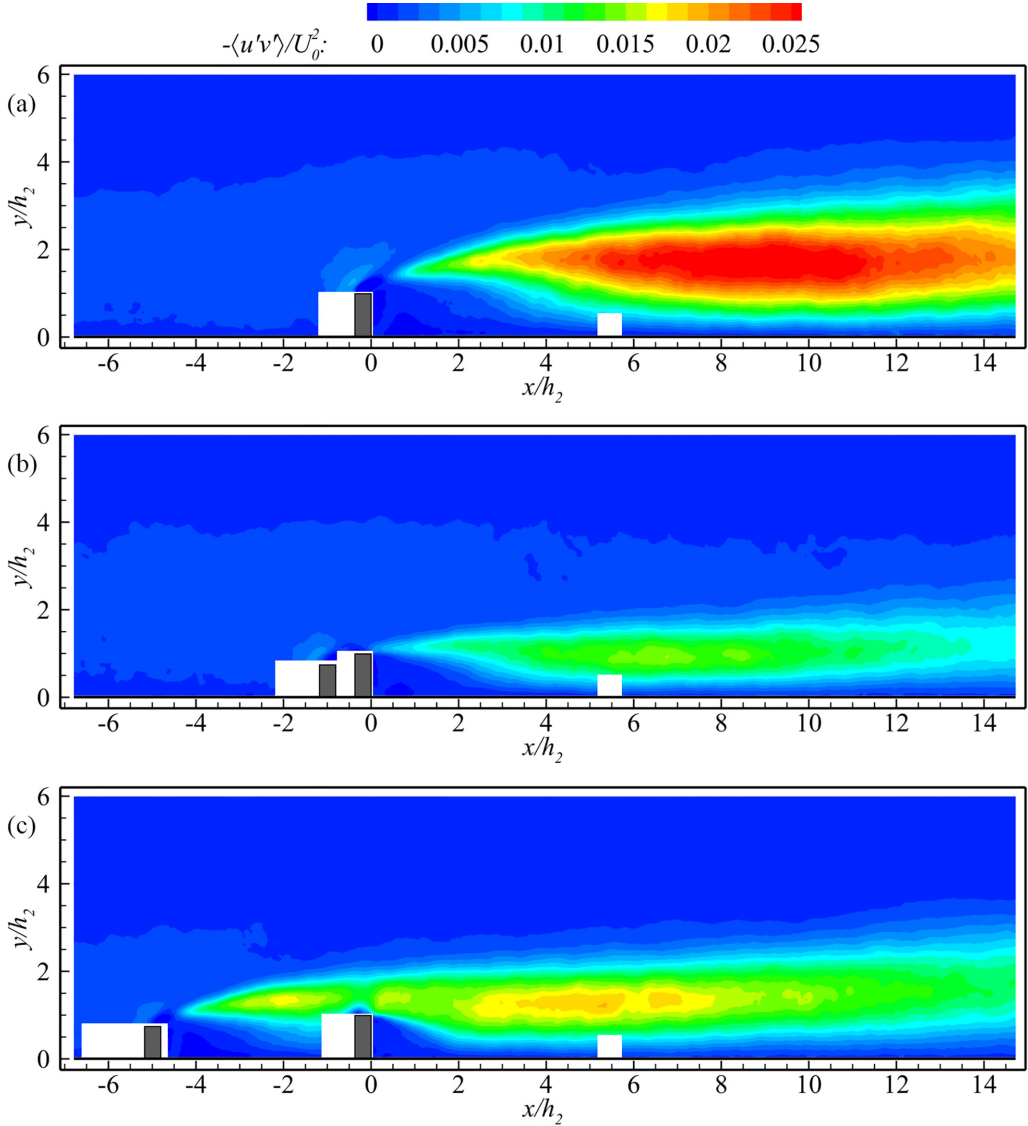
FIG. 10. Contours of the Reynolds shear stress $-\langle u'v' \rangle / U_0^2$ for (a) the isolated bar case; (b) the $l/h_2 = 0.8$, $h_1/h_2 = 0.75$ case; and (c) the $l/h_2 = 4.8$, $h_1/h_2 = 0.75$ case.

case at $x/h_2 = 2$. As noted earlier, the maximum Reynolds shear stress is reduced, to various degrees, in all two-bar cases relative to the isolated bar case. As the shear layer grows with x/h_2, nonzero $\Delta(-u'v')/U_0^2$ penetrates deeper within the boundary layer; overall, this penetration is reduced for cases with $h_1/h_2 < 1$ likely due to the more gradual upward flow deflection evidenced by the reduced V/U_0 (Fig. 6). In particular, introducing an upstream bar with $h_1/h_2 = 0.75$ at $0.8 \leqslant l/h_2 \leqslant 4.8$ is effective in reducing the perturbation of incoming boundary layer turbulence in both extent and magnitude.

Despite the incoming turbulence, the flow past the isolated bar is populated by coherent large-scale vortical structures, which are visualized at two nonconsecutive instants in Fig. 12. These visualizations, obtained via the volumetric flow measurements, are deemed representative based on observations of a large number of instantaneous fields. Figures 12(a) and 12(b) show
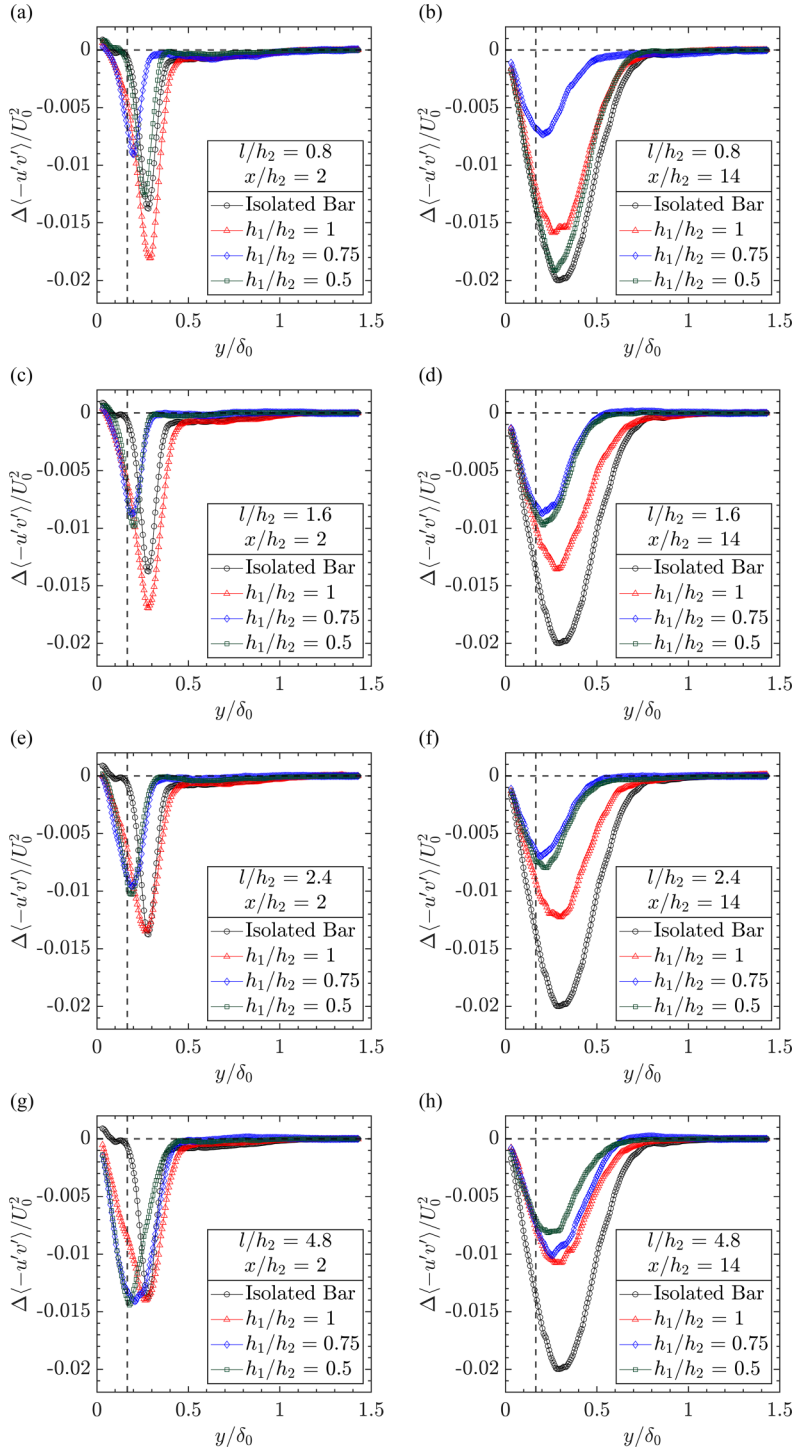
FIG. 11. Wall-normal profiles of the Reynolds shear stress deficit relative to the unperturbed boundary layer $\Delta\langle -u'v'\rangle/U_0^2$ at $x/h_2 = 2$ (left) and $x/h_2 = 14$ (right): (a) and (b) $l/h_2 = 0.8$, (c) and (d) $l/h_2 = 1.6$, (e) and (f) $l/h_2 = 2.4$, and (g) and (h) $l/h_2 = 4.8$. The vertical dashed line at $y/\delta_0 = 0.17$ indicates the top of the downstream bar. The isolated bar case is shown in all subfigures to aid in comparison.
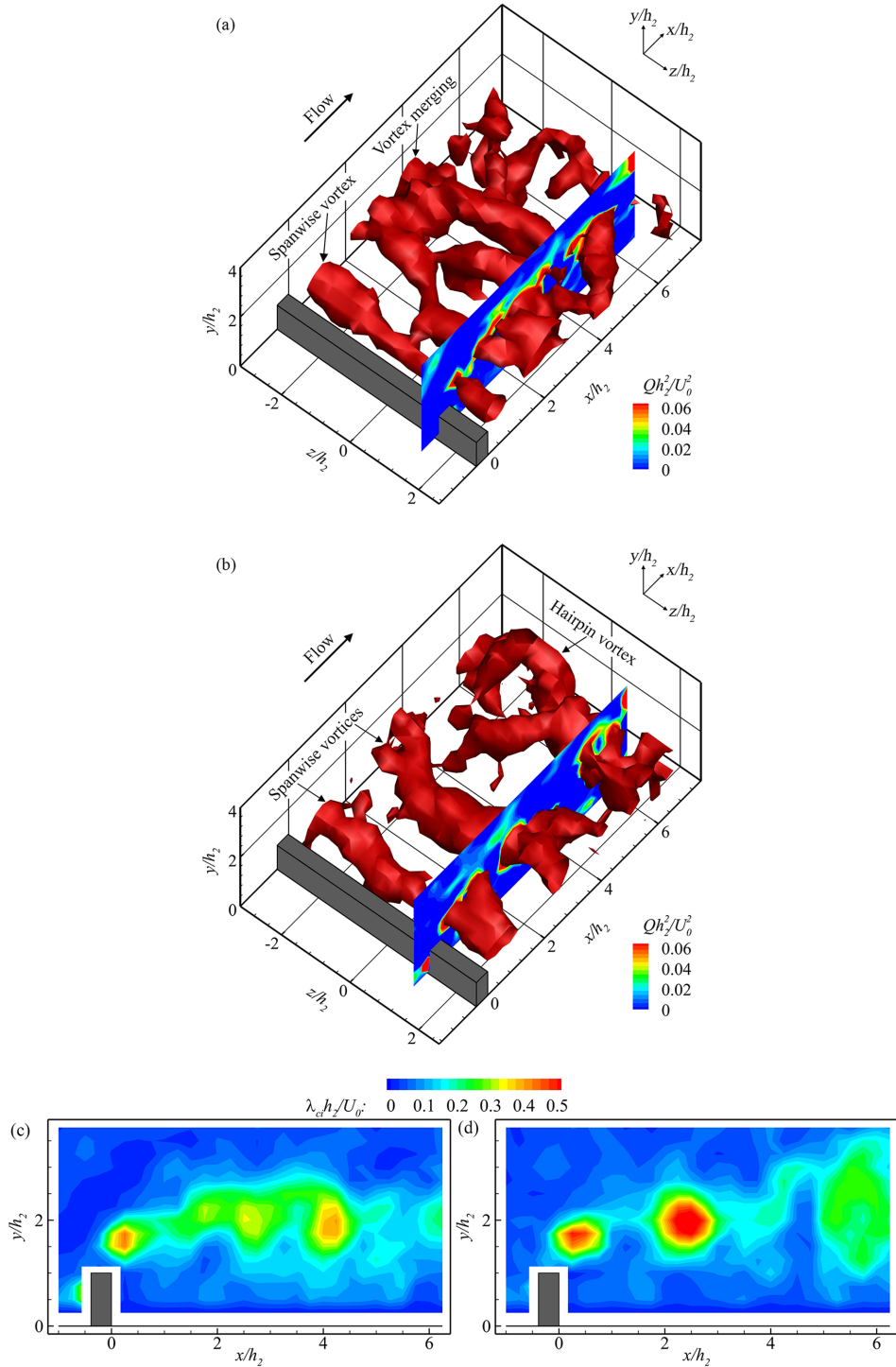
FIG. 12. Visualizations of the vortical structures past the isolated bar at two representative, nonconsecutive instants. (a),(b) Isosurfaces of the swirling strength $\lambda_{ci}h_2/U_0 = 0.28$ along with contours of the Q-criterion Qh_2^2/U_0^2 within a streamwise-wall-normal plane. (c),(d) Contours of the spanwise-averaged swirling strength $\lambda_{ci}h_2/U_0$ at the same instants as in (a) and (b), respectively.

isosurfaces of the swirling strength $\lambda_{ci} h_2/U_0 = 0.28$ intersected by a streamwise-wall-normal plane with contours of the Q-criterion, Qh_2^2/U_0^2. Figures 12(c) and 12(d) provide the spanwise-averaged swirling strength $\lambda_{ci} h_2/U_0$ distribution at the same instants as in Figs. 12(a) and 12(b), respectively. The swirling strength $\lambda_{ci} h_2/U_0$ is defined as the magnitude of the imaginary part of the complex eigenvalues of the local velocity gradient tensor [86], and Qh_2^2/U_0^2 is the second invariant of the local velocity gradient tensor [87]. As shown in Figs. 12(a) and 12(b), there is agreement between the two vortex-identification methods. Moreover, visualizations of the λ_2-criterion were also in agreement; λ_2 is defined as the second largest eigenvalue of the sum of the square of the symmetric and antisymmetric components of the velocity gradient tensor [88]. Since these vortex identification methods are sensitive to the level chosen for isosurfaces, multiple levels were visualized to ensure that the discussion presented below is robust. Past the isolated bar, spanwise vortices form due to the roll up of the shear layer and grow as they advect downstream [Figs. 12(a) and 12(b)]. Near the bar, these vortices exhibit more two-dimensionality and less spanwise variation relative to downstream locations. As the spanwise vortices advect downstream, they often merge/pair at one or multiple spanwise locations [Fig. 12(a)]. They are also often lifted at a spanwise location, forming an archlike or hairpinlike structure such as the one shown in Fig. 12(b). The spanwise vortices and their growth, interactions, and evolution are similar to those noted in recent numerical simulations of flow over 2D bars subjected to uniform flow or thin boundary layers [44–47]. In comparison to these studies, the isolated bar considered here is subjected to the relatively high shear and turbulence associated with the lower portion of the incoming turbulent boundary layer. Relative to the results in Refs. [44–47], the incoming flow turbulence appears to increase spanwise variations in the spanwise vortices and shorten the streamwise extent in which they are 2D. Across the four cases investigated via volumetric measurements (isolated bar and three two-bar cases: $l/h_2 = 0.8$, 1.6, and 4.8 with $h_1/h_2 = 0.75$), spectral analysis of the spanwise-averaged swirling strength $\lambda_{ci} h_2/U_0$ at $(x/h_2, y/h_2) = (2.75, 2)$ indicates a dominant peak at a frequency f associated with the Strouhal number $St = fh_2/U_0$ in the range 0.12–0.15, likely associated with spanwise vortices. Additional measurements are needed to discern the differences in St across the considered cases. The obtained St range agrees well with $St = 0.12$ reported by Güemes *et al.* [35] for the shedding past an isolated 2D bar immersed in a turbulent boundary layer and occupying 35% of its thickness; their spectral analysis was performed in the near wake and at a similar height but on the streamwise velocity.

Sheltering by an upstream bar induces more spanwise variations and three-dimensionality in the vortical structures observed in the downstream bar wake, likely through interactions with the shear layer stemming from the upstream bar. Across the three two-bar cases investigated via volumetric flow measurements ($l/h_2 = 0.8$, 1.6, and 4.8 with $h_1/h_2 = 0.75$), the $l/h_2 = 4.8$, $h_1/h_2 = 0.75$ case shows the most 3D vortical structures. Two representative fields for this case are provided in Fig. 13, where swirling strength $\lambda_{ci} h_2/U_0$ isosurfaces and contours highlight the increased three-dimensionality. While spanwise vortices are still observed past the downstream bar, they extend for shorter spanwise lengths and exhibit more three-dimensionality. Additionally, hairpin structures occur more frequently. In Fig. 13(a), two hairpin vortices are shown: one is completely in the measurement volume, while the head of the other is outside (but was seen within the measurement volume in earlier instants). In Fig. 13(b), a group of three hairpin structures are observed just downstream of a spanwise vortex. In addition to the spanwise and hairpin vortices, quasistreamwise vortices occur frequently; however, they could be the legs of hairpin structures not fully captured within the measurement volume. The increase in the three-dimensionality of the vortical structures is also evidenced by comparing the spanwise-averaged $\lambda_{ci} h_2/U_0$ distributions in Figs. 12 and 13, where the compact signature of the spanwise vortices shown for the isolated bar case is significantly reduced for the $l/h_2 = 4.8$, $h_1/h_2 = 0.75$ case. It is likely that some of the hairpin structures observed in the downstream bar wake originate as spanwise vortices past the upstream bar: these spanwise vortices are lifted at spanwise locations to form hairpin vortices, which are then advected downstream. It is also possible that some of the hairpin structures originate as spanwise vortices at the downstream bar and become 3D over a shorter streamwise distance due to interactions
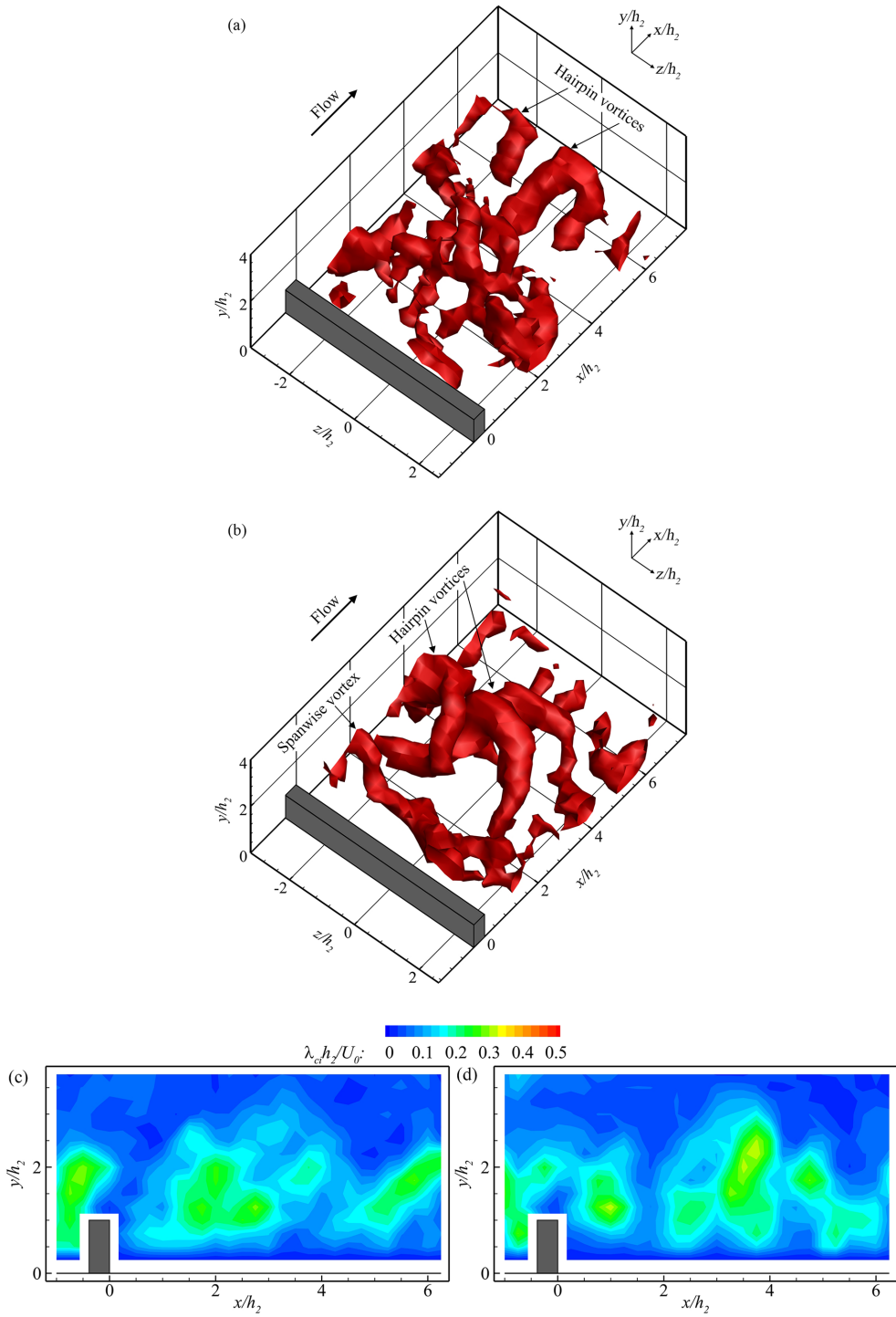
FIG. 13. Visualizations of the vortical structures past the downstream bar for the $l/h_2 = 4.8$, $h_1/h_2 = 0.75$ case at two representative, nonconsecutive instants. (a),(b) Isosurfaces of the swirling strength $\lambda_{ci}h_2/U_0 = 0.28$. (c),(d) Contours of the spanwise-averaged swirling strength $\lambda_{ci}h_2/U_0$ at the same instants as in (a) and (b), respectively.
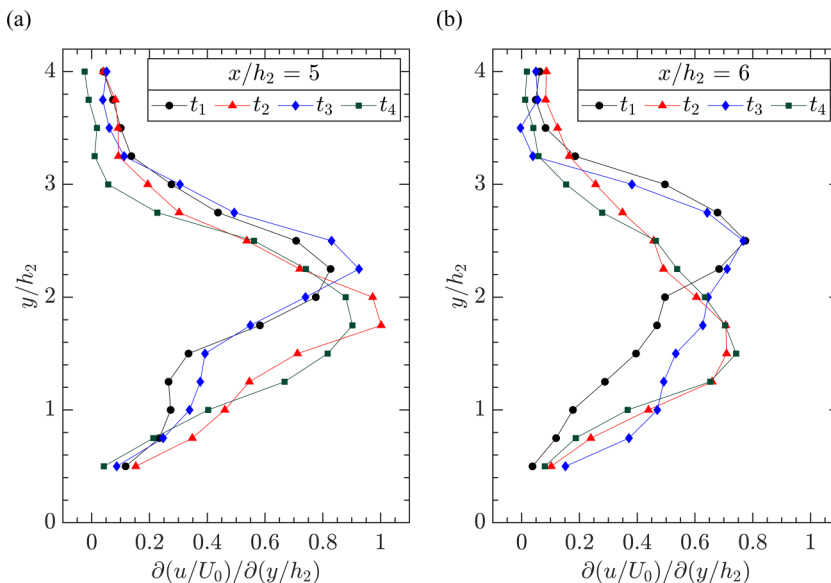
FIG. 14. Wall-normal profiles of the instantaneous spanwise-averaged vertical shear $\partial(u/U_0)/\partial(y/h_2)$ for the isolated bar case at four select, nonconsecutive instants $t_1 - t_4$. The profiles highlight the shear layer flapping at (a) $x/h_2 = 5$ and (b) $x/h_2 = 6$.

with the upstream bar wake. While the measurements highlight the increased three-dimensionality in the downstream bar wake due to sheltering, additional measurements are needed to pinpoint the interactions between the vortices shed from the two bars. Specifically, measurements within volumes containing both bars across a wide range of l/h_2 and h_1/h_2 would aid in addressing vortical structure interactions.

In addition to the shedding of large-scale vortical structures, the shear layer undergoes a flapping motion as previously found past backward-facing steps (e.g., Refs. [39–43]) and past an isolated 2D bar extending beyond the boundary layer thickness [38]. To quantitatively describe this flapping motion, Fig. 14 provides wall-normal profiles of select instantaneous spanwise-averaged vertical shear $\partial(u/U_0)/\partial(y/h_2)$ at $x/h_2 = 5$ and 6 for the isolated bar case. Four instants are chosen to illustrate the maximum vertical extent of the flapping motion. At $x/h_2 = 6$ [Fig. 14(b)], for example, the maximum and minimum heights of the peak spanwise-averaged $\partial(u/U_0)/\partial(y/h_2)$ across the dataset are $y/h_2 = 2.5$ and 1.5, respectively. The maximum vertical flapping extent is defined as the distance between these maximum and minimum heights; for the isolated bar case, this extent is $1.0h_2$. The flapping behavior is observed in all cases investigated via volumetric flow measurements; at $x/h_2 = 6$, the maximum vertical flapping extent for the $h_1/h_2 = 0.75$ cases varies from $0.8h_2$ (for $l/h_2 = 0.8$ and 1.6) to $1.5h_2$ (for $l/h_2 = 4.8$). The flapping motion and its maximum vertical extent are modulated by the shear layer stemming from the upstream bar and the vortical structure in the upstream and downstream bar wakes. Measurements within volumes containing both bars across the range of l/h_2 and h_1/h_2 would illustrate the effects of the upstream shear layer and vortical structures on the flapping motion. Additionally, for cases where reattachment occurs within the measurement volume, spanwise variations in the reattachment location and streamwise variations in the spanwise-averaged reattachment location are observed as in the flow over a backward-facing step.
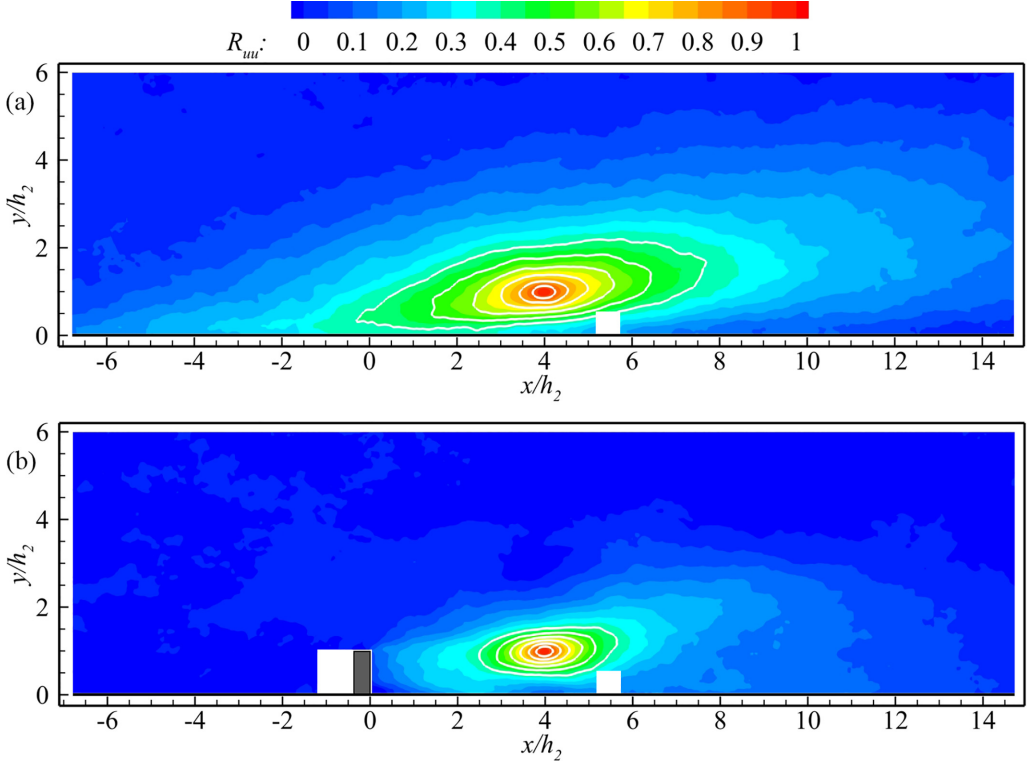
FIG. 15. Contours of the two-point correlation R_{uu} at $(x_{ref}, y_{ref}) = (4h_2, h_2)$ for (a) the unperturbed boundary layer and (b) the isolated bar case. $y_{ref} = h_2$ corresponds to $0.17\delta_0$. White contours at correlation levels 0.4–0.9 are shown in 0.1 increments to aid in comparison.

The bar-induced changes to the turbulence structure of the boundary layer are investigated through the two-point, one-time fluctuating velocity correlation

$$R_{uu} = \frac{\langle u'(x_{ref}, y_{ref}) u'(x, y) \rangle}{\langle u'^2(x_{ref}, y_{ref}) \rangle^{1/2} \langle u'^2(x, y) \rangle^{1/2}}, \tag{1}$$

shown in Fig. 15 for the unperturbed boundary layer and the isolated bar case. R_{uu} is calculated using the large FOV PIV flow fields, and the reference point is $(x_{ref}, y_{ref}) = (4h_2, h_2)$, which corresponds to approximately the center of the FOV in the streamwise direction and $y/\delta_0 = 0.17$. For the unperturbed boundary layer [Fig. 15(a)], R_{uu} is elongated in the streamwise direction with an inclination away from the wall at the downstream side. This R_{uu} distribution is consistent with that over smooth and rough walls reported in the literature and has been associated with hairpin vortex packets (see, for example, Fig. 9 and associated discussion in Ref. [89]). The region with elevated R_{uu} is significantly altered due to the perturbation by the isolated bar [Fig. 15(b)]; specifically, the streamwise and wall-normal extents of the highly correlated R_{uu} region are significantly reduced. The modification to R_{uu} suggests a disturbance to the boundary layer turbulence structure through the generation of new coherent vortical structures associated with the shear layer past the bar. An R_{uu} distribution similar to that in Fig. 15(b) is observed for all two-bar cases; however, the size of the highly correlated region varies with l/h_2 and h_1/h_2. This size is examined through the maximum streamwise extent of the $R_{uu} = 0.5$ contour, denoted as l_{uu}/h_2; Fig. 16 provides l_{uu}/h_2 for $y_{ref}/h_2 = 1$ and $x_{ref}/h_2 = 2, 4, 6, 8, 10,$ and 12. For the unperturbed boundary layer, l_{uu}/h_2 remains constant near 5.3 (represented as a dashed line in Fig. 16). For the isolated bar case, the highly correlated region grows such that l_{uu}/h_2 increases from 1.7 to 3.0 over a streamwise
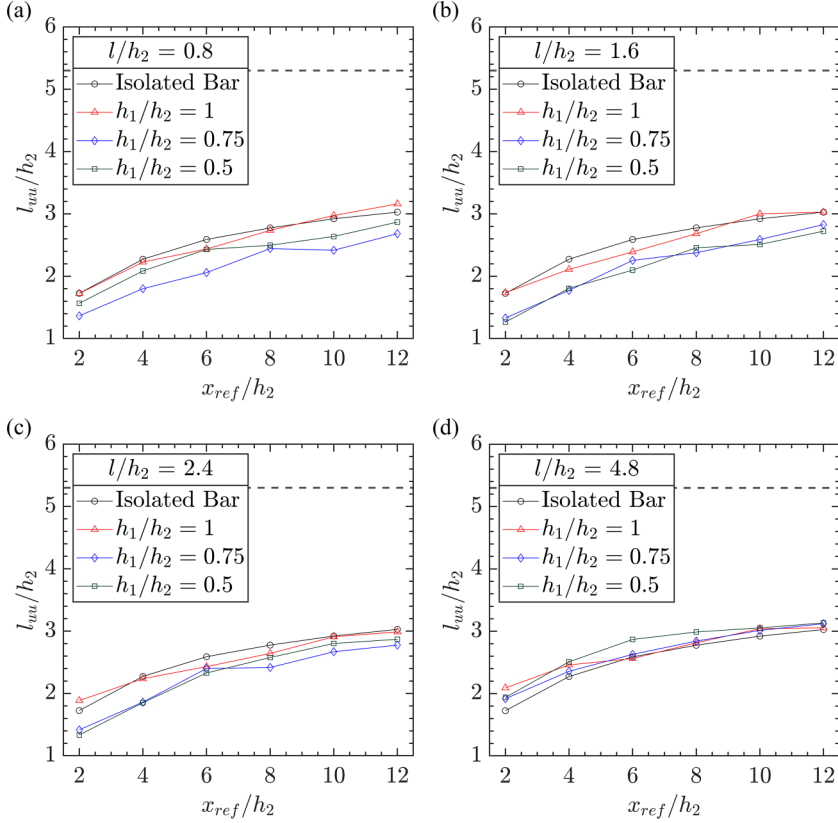
FIG. 16. Streamwise extent of the $R_{uu} = 0.5$ contour (l_{uu}/h_2) at $y_{\mathrm{ref}}/h_2 = 1$ ($y/\delta_0 = 0.17$): (a) $l/h_2 = 0.8$, (b) $l/h_2 = 1.6$, (c) $l/h_2 = 2.4$, (d) $l/h_2 = 4.8$. The dashed line at $l_{uu}/h_2 = 5.3$ indicates the extent of the $R_{uu} = 0.5$ contour for the unperturbed boundary layer. The isolated bar case is shown in all subfigures to aid in comparison.

distance of $10h_2$; this growth is associated with the growth of the shear layer (Figs. 3 and 10) and its coherent vortical structures (Fig. 12). Similarly, l_{uu}/h_2 grows over x/h_2 for the two-bar cases but remains significantly below l_{uu}/h_2 for the unperturbed boundary layer (Fig. 16). For the $l/h_2 = 0.8$, 1.6, and 2.4 cases [Figs. 16(a)–16(c)], l_{uu}/h_2 for the isolated bar is generally near or above that of the two-bar cases, despite the distance available for growth for the upstream bar shear layer. The effect of the upstream shear layer growth on l_{uu}/h_2 is noted for the $l/h_2 = 4.8$ cases [Fig. 16(d)], where l_{uu}/h_2 for the isolated bar is generally near or below that of the two-bar cases. The maximum wall-normal extent of the $R_{uu} = 0.5$ contour (not shown for brevity) exhibits similar features to those of the maximum streamwise extent in Fig. 16. Specifically, the maximum wall-normal extent for the isolated bar case and all two-bar cases is below that of the unperturbed boundary layer. The maximum wall-normal extent increases with x/h_2, but in an approximately linear trend. Moreover, the maximum wall-normal extent exhibits a similar dependency on l/h_2 as in Fig. 16. For the isolated bar case, the R_{uu} distribution at a reference point with the same height as in Fig. 15 and $\sim 1.5h_2$ upstream of the bar (not shown for brevity) exhibits a highly correlated region similar in streamwise extent to that in Fig. 15(a). However, the highly correlated region has a significantly larger inclination, suggesting a possible lifting up of the incoming flow structures due to the bar-induced intense upwash. An increase in the inclination is also observed upstream of the upstream bar for the two-bar cases where the FOV extends sufficiently upstream to calculate R_{uu}. Relative to the unperturbed boundary layer, the changes to R_{uu} (Figs. 15 and 16)

and the change in the lengthscale and energy of low-order proper orthogonal decomposition (POD) modes (see the Appendix for further details) suggest that the bar(s) weaken the large-scale structures associated with the incoming flow, likely through the impact of the bar(s) on the flow field (e.g., the intense upwash and large flow recirculation) and through the generation of new large-scale vortical structures such as the ones visualized in Figs. 12 and 13.

IV. CONCLUSIONS

The turbulent flow over isolated and sheltered 2D bar roughness elements was experimentally investigated using planar PIV and volumetric PTV. The bar(s) occupied up to 17% of the incoming turbulent boundary layer thickness and, therefore, were subjected to the high shear and turbulence associated with the incoming flow. To examine the effects of sheltering by an upstream bar, the flow over two bars positioned in close proximity was investigated at various streamwise spacings l/h_2 and height ratios h_1/h_2. For the considered spacings ($0.8 \leqslant l/h_2 \leqslant 4.8$), flow recirculation occupies the entire cavity between the two bars and exhibits patterns dependent on both l/h_2 and h_1/h_2. While the large-scale flow features are qualitatively similar for the two-bar cases and the isolated bar case (e.g., flow deceleration, upwash, downwash, and flow recirculation), significant quantitative differences are noted in important quantities such as the reattachment length, velocity deficit, wall-normal velocity, and vertical extent of the boundary layer perturbation. The reattachment length past the downstream bar is highly dependent on both l/h_2 and h_1/h_2, suggesting opportunities for control of flow over isolated bars. For example, the introduction of a bar at $l/h_2 = 0.8$ with $h_1/h_2 = 0.75$ reduces the reattachment length from $11.0h_2$ for the isolated bar to $6.7h_2$ for the sheltered bar. Sheltering by an upstream bar also modulates the response of the incoming turbulent boundary layer. Specifically, the flow deflection at the bars, characterized by the time-averaged wall-normal velocity, is significantly reduced for the $h_1/h_2 < 1$ cases. Similarly, the flow deficit in the wake of the downstream bar is reduced for sheltered bars. Sheltering appears to impact the wake and reattachment past the downstream bar through multiple mechanisms including the more gradual flow deflection for upstream bars with $h_1/h_2 < 1$, the enhanced turbulence and entrainment associated with the upstream bar shear layer, and the structure and vertical extent of the recirculation flow between the two bars. These mechanisms, which influence the flow organization past the downstream bar, are highly dependent on both l/h_2 and h_1/h_2.

Turbulence levels are elevated within the shear layers past the upstream and downstream bars with a peak occurring past the downstream bar. The Reynolds shear stress $-\langle u'v' \rangle/U_0^2$ is reduced due to sheltering. For example, the maximum $-\langle u'v' \rangle/U_0^2$ for an isolated bar is reduced by 45% due to the introduction of an upstream bar at $l/h_2 = 0.8$ with $h_1/h_2 = 0.75$. Moreover, sheltering by an upstream bar with $h_1/h_2 < 1$ reduces the wall-normal extent of the boundary layer perturbation, as noted in profiles of the Reynolds shear stress $-\langle u'v' \rangle/U_0^2$ deficit relative to the unperturbed boundary layer. Visualizations of the vortical structures past the isolated bar indicate the presence of coherent spanwise vortices that grow as they advect downstream. These spanwise vortices often merge/pair and evolve into arch or hairpin structures; such interactions result in a loss of two-dimensionality. Sheltering by an upstream bar enhances such interactions and loss of two-dimensionality. In addition to the shedding of large-scale vortical structures, the shear layer past the downstream bar undergoes a flapping motion similar to shear layers past backward-facing steps. The bar(s) alter the turbulence structure of the boundary layer as indicated by two-point correlations and POD analyses, which suggest a weakening of the large-scale structures of the incoming turbulent boundary layer. The change in the boundary layer turbulence structure is associated with the significant impact of the bar(s) on the flow field (e.g., the intense upwash and flow recirculation) and the generation of new coherent vortical structures in the shear layers past the bars. Overall, the results highlight significant changes to the downstream bar wake due to sheltering by an upstream bar; these changes are highly dependent on both h_1/h_2 and l/h_2. Future efforts will investigate which, if any, of these sheltering effects apply locally within the roughness sublayer of flow over periodic 2D bars.

APPENDIX: POD ANALYSIS

In this Appendix, the effects of the isolated and sheltered bars on the boundary layer turbulence structure are investigated through snapshot proper orthogonal decomposition (POD) applied to the in-plane fluctuating velocity fields $\mathbf{u}'(\mathbf{x}, t) = u'(\mathbf{x}, t)\hat{i} + v'(\mathbf{x}, t)\hat{j}$ obtained via the large FOV PIV measurements. Following Sirovich [90], $\mathbf{u}'(\mathbf{x}, t)$ is decomposed into a deterministic part $\boldsymbol{\phi}^n(\mathbf{x})$ (often referred to as spatial modes, eigenmodes, or POD modes) and time-dependent coefficients $a^n(t)$ as

$$\mathbf{u}'(\mathbf{x}, t) = \sum_{n=1}^{N} a^n(t)\boldsymbol{\phi}^n(\mathbf{x}), \tag{A1}$$

where $N = 4000$ is the total number of velocity fields (snapshots), and the bold symbols denote vectorial quantities. The POD modes are not themselves coherent structures; however, they provide insight into the spatial flow scales and their energies. Here, the modes are ranked in descending order based on their individual energy, as typically done in the literature; the sum of the individual energies is representative of the turbulent kinetic energy of the flow. The low-order POD modes (more energetic modes) exhibit larger spatial structure than the high-order modes (less energetic modes). For additional details on the POD procedure and interpretation, the reader is referred to, for example, Refs. [62,75,90–92]. Table I provides the individual energy for each of the first four POD modes (E_1–E_4) as well as the cumulative energy of the first four and ten modes ($\sum E_{1-4}$ and $\sum E_{1-10}$); these energies are reported as a percentage of the total energy. The table also lists the total number of modes M containing 75% of the total energy. The low-order POD modes for the isolated bar case deviate in structure from those of the unperturbed boundary layer, which is in line with results reported by, for example, Shah and Tachie [32], Güemes *et al.* [35], and Mallor *et al.* [34]. The energies of the first four modes for the isolated bar case are similar to those of the unperturbed boundary layer; however, their lengthscales differ, suggesting changes to the turbulence structure of the boundary layer due to the shear layer, which is a dominant feature of the flow field (Figs. 3 and 10). The POD modes are not shown for brevity; the reader is referred to Güemes *et al.* [35] and Mallor *et al.* [34] for visualizations in line with the results obtained here. These visualizations evidence energetic low-order modes that are associated with the bar shear layer [34,35]. Additionally, perturbing the boundary layer by an isolated bar reduces M from 128 to 96; this reduction suggests a redistribution of the energy toward the lower-order modes associated with the shear layer past the bar. Relative to the isolated bar case, the shear layer past the downstream bar in the two-bar cases remains a governing feature of the flow (Figs. 4 and 10); however, the associated turbulence is reduced, and the spanwise vortical structures lose coherence. As the shear layer and associated vortical structures become less pronounced, the low-order modes associated with the shear layer become less energetic compared to the isolated bar case (Table I), and more modes are required to achieve a certain threshold of cumulative energy (i.e., M is increased). The decrease in the energies of low-order modes and the increase in M for the two-bar cases relative to the isolated bar case is in line with the observations of the vortical structures discussed in the context of Fig. 13.

TABLE I. Individual energies of the first four POD modes as a percentage of the total energy (E_1–E_4), the cumulative energy of the first four and ten modes as a percentage of the total energy ($\sum E_{1-4}$ and $\sum E_{1-10}$), and the number of modes M containing 75% of the total energy.

Case		E_1 (%)	E_2 (%)	E_3 (%)	E_4 (%)	$\sum E_{1-4}$ (%)	$\sum E_{1-10}$ (%)	M
Unperturbed boundary layer		12.3	8.0	5.1	4.0	29.5	42.8	128
Isolated bar		11.6	8.0	5.6	3.9	29.1	43.6	96
$l/h_2 = 0.8$	$h_1/h_2 = 1$	10.4	7.9	5.1	3.8	27.3	41.8	105
	$h_1/h_2 = 0.75$	8.1	5.9	5.5	3.5	22.9	36.7	146
	$h_1/h_2 = 0.5$	10.8	8.0	5.7	3.7	28.1	42.7	100
$l/h_2 = 1.6$	$h_1/h_2 = 1$	9.7	7.3	4.7	4.0	25.7	39.7	119
	$h_1/h_2 = 0.75$	8.4	6.6	5.1	4.6	24.5	38.6	135
	$h_1/h_2 = 0.5$	8.5	6.7	5.1	4.4	24.7	39.0	130
$l/h_2 = 2.4$	$h_1/h_2 = 1$	9.0	6.9	4.5	4.3	24.6	38.4	133
	$h_1/h_2 = 0.75$	8.2	5.8	5.3	3.8	23.1	36.7	150
	$h_1/h_2 = 0.5$	8.9	6.2	5.2	3.9	24.3	37.9	144
$l/h_2 = 4.8$	$h_1/h_2 = 1$	9.2	6.5	4.3	3.7	23.7	36.6	150
	$h_1/h_2 = 0.75$	9.2	7.3	4.8	3.7	25.0	38.5	129
	$h_1/h_2 = 0.5$	9.0	6.9	4.5	4.3	24.6	38.4	131

[1] A. E. Perry, W. H. Schofield, and P. N. Joubert, Rough wall turbulent boundary layers, J. Fluid Mech. **37**, 383 (1969).

[2] P.-Å. Krogstad, H. I. Andersson, O. M. Bakken, and A. Ashrafian, An experimental and numerical study of channel flow with rough walls, J. Fluid Mech. **530**, 327 (1999).

[3] M. F. Tachie, M. Agelinchaab, and M. K. Shah, Turbulent flow over transverse ribs in open channel with converging side walls, Int. J. Heat Fluid Flow **28**, 683 (2007).

[4] R. J. Volino, M. P. Schultz, and K. A. Flack, Turbulence structure in a boundary layer with two-dimensional roughness, J. Fluid Mech. **635**, 75 (2009).

[5] M. F. Tachie, S. S. Paul, M. Agelinchaab, and M. K. Shah, Structure of turbulent flow over 90 and 45 transverse ribs, J. Turbul. **10**, N20 (2009).

[6] V. Roussinova and R. Balachandar, Open channel flow past a train of rib roughness, J. Turbul. **12**, N28 (2011).

[7] J. H. Lee, A. Seena, S. H. Lee, and H. J. Sung, Turbulent boundary layers over rod-and cube-roughened walls, J. Turbul. **13**, N40 (2012).

[8] X. Fang, Z. Yang, B. C. Wang, M. F. Tachie, and D. J. Bergstrom, Highly-disturbed turbulent flow in a square channel with v-shaped ribs on one wall, Int. J. Heat Fluid Flow **56**, 182 (2015).

[9] J. Lee, J. H. Kim, and J. H. Lee, Scale growth of structures in the turbulent boundary layer with a rod-roughened wall, Phys. Fluids **28**, 015104 (2016).

[10] Y. K. Choi, H. G. Hwang, Y. M. Lee, and J. H. Lee, Effects of the roughness height in turbulent boundary layers over rod-and cuboid-roughened walls, Int. J. Heat Fluid Flow **85**, 108644 (2020).

[11] A. M. Hamed, C. E. Nye, and A. J. Hall, Effects of localized blowing on the turbulent boundary layer over 2d roughness, Exp. Fluids **62**, 1 (2021).

[12] S. Leonardi, P. Orlandi, R. J. Smalley, L. Djenidi, and R. A. Antonia, Direct numerical simulations of turbulent channel flow with transverse square bars on one wall, J. Fluid Mech. **491**, 229 (2003).

[13] S. Leonardi, P. Orlandi, L. Djenidi, and R. A. Antonia, Structure of turbulent channel flow with square bars on one wall, Int. J. Heat Fluid Flow **25**, 384 (2004).

[14] S. Leonardi, P. Orlandi, and R. A. Antonia, Properties of d- and k-type roughness in a turbulent channel flow, Phys. Fluids **19**, 125101 (2007).

[15] S. H. Lee and H. J. Sung, Direct numerical simulation of the turbulent boundary layer over a rod-roughened wall, J. Fluid Mech. **584**, 125 (2007).

[16] L. Djenidi, R. A. Antonia, M. Amielh, and F. Anselmet, A turbulent boundary layer over a two-dimensional rough wall, Exp. Fluids **44**, 37 (2007).

[17] R. J. Volino, M. P. Schultz, and K. A. Flack, Turbulence structure in boundary layers over periodic two- and three-dimensional roughness, J. Fluid Mech. **676**, 172 (2011).

[18] J. Jimenez, Turbulent flows over rough walls, Annu. Rev. Fluid Mech. **36**, 173 (2004).

[19] P.-Å. Krogstad and V. Efros, About turbulence statistics in the outer part of a boundary layer developing over two-dimensional surface roughness, Phys. Fluids **24**, 075112 (2012).

[20] K. A. Flack and M. P. Schultz, Roughness effects on wall-bounded turbulent flows, Phys. Fluids **26**, 101305 (2014).

[21] D. Chung, N. Hutchins, M. P. Schultz, and K. A. Flack, Predicting the drag of roughness, Annu. Rev. Fluid Mech. **53**, 439 (2021).

[22] J. van der Kindere and B. Ganapathisubramani, Effect of length of two-dimensional obstacles on characteristics of separation and reattachment, J. Wind Eng. Ind. Aerod. **178**, 38 (2018).

[23] H. Chalmers, X. Fang, and M. F. Tachie, Streamwise aspect ratio effects on turbulent flow separations induced by forward–backward-facing steps, J. Fluid Eng. **143**, 021305 (2021).

[24] J. Counihan, J. C. R. Hunt, and P. S. Jackson, Wakes behind two-dimensional surface obstacles in turbulent boundary layers, J. Fluid Mech. **64**, 529 (1974).

[25] S. Acharya, S. Dutta, T. A. Myrum, and R. S. Baker, Turbulent flow past a surface-mounted two-dimensional rib, J. Fluid Eng. **116**, 238 (1994).

[26] M. Agelinchaab and M. F. Tachie, Piv study of separated and reattached open channel flow over surface mounted blocks, J. Fluid Eng. **130**, 061206 (2008).

[27] M. K. Shah and M. F. Tachie, Flow relaxation past a transverse square rib in pressure gradients, AIAA J. **46**, 1849 (2008).

[28] M. K. Shah and M. F. Tachie, Piv investigation of flow over a transverse square rib in pressure gradients, J. Turbul. **10**, N39 (2009).

[29] L. Ding, T. Van Buren, I. E. Gunady, and A. J. Smits, Perspective on the response of turbulent pipe flows to strong perturbations, Fluids **6**, 208 (2021).

[30] S. Goswami and A. Hemmati, Evolution of turbulent pipe flow recovery over a square bar roughness element at a range of reynolds numbers, Phys. Fluids **33**, 035113 (2021).

[31] L. Ding and A. J. Smits, Relaxation of turbulent pipe flow downstream of a square bar roughness element, J. Fluid Mech. **922**, A34 (2021).

[32] M. K. Shah and M. F. Tachie, Proper orthogonal decomposition analysis of separated and reattached pressure gradient flows, AIAA J. **47**, 2616 (2009).

[33] C. He, Y. Liu, D. Peng, and S. Yavuzkurt, Measurement of flow structures and heat transfer behind a wall-proximity square rib using tsp, piv and split-fiber film, Exp. Fluids **57**, 1 (2016).

[34] F. Mallor, M. Raiola, C. Sanmiguel Vila, R. Örlü, S. Discetti, and A. Ianiro, Modal decomposition of flow fields and convective heat transfer maps: An application to wall-proximity square ribs, Exp. Therm. Fluid Sci. **102**, 517 (2019).

[35] A. Güemes, C. Sanmiguel Vila, R. Örlü, R. Vinuesa, P. Schlatter, A. Ianiro, and S. Discetti, Flow organization in the wake of a rib in a turbulent boundary layer with pressure gradient, Exp. Therm. Fluid Sci. **108**, 115 (2019).

[36] F. Li, C. He, P. Wang, and Y. Liu, Unsteady analysis of turbulent flow and heat transfer behind a wall-proximity square rib using dynamic delayed detached-eddy simulation, Phys. Fluids **33**, 055104 (2021).

[37] V. Serta Fraga, G. Yin, and M. C. Ong, Three-dimensional numerical simulations and proper orthogonal decomposition analysis of flow over different bottom-mounted ribs, Ships Offshore Struct. **17**, 792 (2022).

[38] Y. Z. Liu, F. Ke, and H. J. Sung, Unsteady separated and reattaching turbulent flow over a two-dimensional square rib, J. Fluids Struct. **24**, 366 (2008).

[39] H. Le, P. Moin, and J. Kim, Direct numerical simulation of turbulent flow over a backward-facing step, J. Fluid Mech. **330**, 349 (1997).

[40] I. Lee and H. J. Sung, Multiple-arrayed pressure measurement for investigation of the unsteady flow structure of a reattaching shear layer, J. Fluid Mech. **463**, 377 (2002).

[41] W. Hu, S. Hickel, and B. van Oudheusden, Dynamics of a supersonic transitional flow over a backward-facing step, Phys. Rev. Fluids **4**, 103904 (2019).

[42] X. Ma, Z. Tang, and N. Jiang, Eulerian and lagrangian analysis of coherent structures in separated shear flow by time-resolved particle image velocimetry, Phys. Fluids **32**, 065101 (2020).

[43] X. Ma, Z. Tang, and N. Jiang, Investigation of spanwise coherent structures in turbulent backward-facing step flow by time-resolved piv, Exp. Therm. Fluid Sci. **132**, 110569 (2022).

[44] I. E. Abdalla, M. J. Cook, and Z. Yang, Numerical study of transitional separated–reattached flow over surface-mounted obstacles using large-eddy simulation, Int. J. Numer. Meth. Fluids **54**, 175 (2007).

[45] H. Gu, J. Yang, and M. Liu, Study on the instability in separating–reattaching flow over a surface-mounted rib, Int. J. Comput. Fluid Dyn. **31**, 109 (2017).

[46] H. Gu, M. Liu, X. Li, H. Huang, Y. Wu, and F. Sun, The effect of a low-frequency structure on passive scalar transport in the flow over a surface-mounted rib, Flow, Turbul. Combust. **101**, 719 (2018).

[47] G. Yin and M. C. Ong, Numerical analysis on flow around a wall-mounted square structure using dynamic mode decomposition, Ocean Eng. **223**, 108647 (2021).

[48] F. Durst, M. Founti, and S. Obi, Experimental and computational investigation of the two-dimensional channel flow over two fences in tandem, J. Fluid Eng. **110**, 48 (1988).

[49] T. M. Liou, Y. Chang, and D. W. Hwang, Experimental and computational study of turbulent flows in a channel with two pairs of turbulence promoters in tandem, J. Fluid Eng. **112**, 302 (1990).

[50] Y. Chen and K. Wang, Experimental study on the forced convective flow in a channel with heated blocks in tandem, Exp. Therm. Fluid Sci. **16**, 286 (1998).

[51] G. K. Ntinas, I. N. Dados, X. Shen, N. A. Malamataris, V. P. Fragos, and G. Zhang, Characteristics of unsteady flow around two successive rectangular ribs on floor of a wind tunnel, Eur. J. Mech. B Fluids **65**, 450 (2017).

[52] G. Yin, M. Andersen, and M. C. Ong, Numerical simulations of flow around two tandem wall-mounted structures at high reynolds numbers, Appl. Ocean Res. **99**, 102124 (2020).

[53] S. Goswami and A. Hemmati, Response of turbulent pipeflow to multiple square bar roughness elements at high reynolds number, Phys. Fluids **32**, 075110 (2020).

[54] S. Simoëns, M. Ayrault, and J. M. Wallace, The flow across a street canyon of variable width-part 1: Kinematic description, Atmos. Environ. **41**, 9002 (2007).

[55] S. Simoëns and J. M. Wallace, The flow across a street canyon of variable width-part 2:: Scalar dispersion from a street level line source, Atmos. Environ. **42**, 2489 (2008).

[56] C. Le Ribault, I. Vinkovic, and S. Simoëns, Large eddy simulation of particle transport and deposition over multiple 2d square obstacles in a turbulent boundary layer, J. Geophys. Res. Atmos. **126**, e2020JD034461 (2021).

[57] R. J. Martinuzzi and B. Havel, Turbulent flow around two interfering surface-mounted cubic obstacles in tandem arrangement, J. Fluids Eng. **122**, 24 (2000).

[58] R. J. Martinuzzi and B. Havel, Vortex shedding from two surface-mounted cubes in tandem, Int. J. Heat Fluid Flow **25**, 364 (2004).

[59] T. Kim and K. T. Christensen, Flow interactions between streamwise-aligned tandem cylinders in turbulent channel flow, AIAA J. **56**, 1421 (2018).

[60] A. M. Hamed, A. M. Peterlein, and L. V. Randle, Turbulent boundary layer perturbation by two wall-mounted cylindrical roughness elements arranged in tandem: Effects of spacing and height ratio, Phys. Fluids **31**, 065110 (2019).

[61] M. Ikhennicheu, G. Germain, P. Druault, and B. Gaurier, Experimental investigation of the turbulent wake past real seabed elements for velocity variations characterization in the water column. Int. J. Heat Fluid Flow **78**, 108426 (2019).

[62] A. M. Hamed and A. M. Peterlein, Turbulence structure of boundary layers perturbed by isolated and tandem roughness elements, J. Turbul. **21**, 17 (2020).

[63] M. Magnier, P. Druault, and G. Germain, Experimental investigation of upstream cube effects on the wake of a wall-mounted cylinder: Wake rising reduction, tke budget and flow organization, Eur. J. Mech. B Fluids **87**, 92 (2021).

[64] J. Gao, K. Agarwal, and J. Katz, Experimental investigation of the three-dimensional flow structure around a pair of cubes immersed in the inner part of a turbulent channel flow, J. Fluid Mech. **918**, A31 (2021).

[65] X. I. A. Yang, J. Sadique, R. Mittal, and C. Meneveau, Exponential roughness layer and analytical model for turbulent boundary layer flow over rectangular-prism roughness elements, J. Fluid Mech. **789**, 127 (2016).

[66] X. I. A. Yang and C. Meneveau, Large eddy simulations and parameterisation of roughness element orientation and flow direction effects in rough wall boundary layers, J. Turbul. **17**, 1072 (2016).

[67] J. Sadique, X. I. A. Yang, C. Meneveau, and R. Mittal, Aerodynamic properties of rough surfaces with high aspect-ratio roughness elements: Effect of aspect ratio and arrangements, Boundary-Layer Meteorol. **163**, 203 (2017).

[68] A. M. Hamed, A. M. Peterlein, and I. Speck, Characteristics of the turbulent flow within short canopy gaps, Phys. Rev. Fluids **5**, 123801 (2020).

[69] T. Wei, R. Schmidt, and P. McMurtry, Comment on the clauser chart method for determining the friction velocity, Exp. Fluids **38**, 695 (2005).

[70] A. J. Smits, B. J. McKeon, and I. Marusic, High–reynolds number wall turbulence, Annu. Rev. Fluid Mech. **43**, 353 (2011).

[71] I. Marusic, J. P. Monty, M. Hultmark, and A. J. Smits, On the logarithmic region in wall turbulence, J. Fluid Mech. **716**, R3 (2013).

[72] L. Djenidi, K. M. Talluru, and R. A. Antonia, A velocity defect chart method for estimating the friction velocity in turbulent boundary layers, Fluid Dyn. Res. **51**, 045502 (2019).

[73] K. A. Flack, M. P. Schultz, and T. A. Shapiro, Experimental support for townsend's reynolds number similarity hypothesis on rough walls, Phys. Fluids **17**, 035102 (2005).

[74] C. Manes, D. Poggi, and L. Ridolfi, Turbulent boundary layers over permeable walls: Scaling and near wall structure, J. Fluid Mech. **687**, 141 (2011).

[75] M. Placidi and B. Ganapathisubramani, Effects of frontal and plan solidities on aerodynamic parameters and the roughness sublayer in turbulent boundary layers, J. Fluid Mech. **782**, 541 (2015).

[76] P. Schlatter and R. Örlü, Assessment of direct numerical simulation data of turbulent boundary layers, J. Fluid Mech. **659**, 116 (2010).

[77] A. Gorbushin, S. Osipova, and V. Zametaev, Mean parameters of an incompressible turbulent boundary layer on the wind tunnel wall at very high reynolds numbers, Flow, Turbul. Combust. **107**, 31 (2021).

[78] K. Christensen, The influence of peak-locking errors on turbulence statistics computed from piv ensembles, Exp. Fluids **36**, 484 (2004).

[79] A. Prasad, R. Adrian, C. Landreth, and P. Offutt, Effect of resolution on the speed and accuracy of particle image velocimetry interrogation, Exp. Fluids **13**, 105 (1992).

[80] A. Boomsma and D. Troolin, Time-resolved particle image identification and reconstruction for volumetric 4d-ptv, in *19th International Symposium on Applications of Laser Techniques to Fluid Mechanics, Lisbon, Portugal* (2018).

[81] D. C. Barros, Y. Duan, D. R. Troolin, and E. K. Longmire, Air-filled soap bubbles for volumetric velocity measurements, Exp. Fluids **62**, 1 (2021).

[82] A. M. Hamed, A. Pagan-Vazquez, D. Khovalyg, Z. Zhang, and L. P. Chamorro, Vortical structures in the near wake of tabs with various geometries, J. Fluid Mech. **825**, 167 (2017).

[83] J. C. Lin, Review of research on low-profile vortex generators to control boundary-layer separation, Prog. Aerosp. Sci. **38**, 389 (2002).

[84] H. Park, W. Jeon, H. Choi, and J. Y. Yoo, Mixing enhancement behind a backward-facing step using tabs, Phys. Fluids **19**, 105103 (2007).

[85] X. Ma, R. Geisler, and A. Schröder, Experimental investigation of three-dimensional vortex structures downstream of vortex generators over a backward-facing step, Flow, Turbul. Combust. **98**, 389 (2017).

[86] J. Zhou, R. J. Adrian, S. Balachandar, and T. M. Kendall, Mechanisms for generating coherent packets of hairpin vortices in channel flow, J. Fluid Mech. **387**, 353 (1999).

[87] J. C. R. Hunt, A. A. Wray, and P. Moin, Eddies, streams, and convergence zones in turbulent flows, Center for Turbulence Research, Proceedings of the Summer Program 1988, Report CTR-S88, 193 (1988), https://ntrs.nasa.gov/citations/19890015184.

[88] J. Jeong and F. Hussain, On the identification of a vortex, J. Fluid Mech. **285**, 69 (1995).

[89] Y. Wu and K. T. Christensen, Spatial structure of a turbulent boundary layer with irregular surface roughness, J. Fluid Mech. **655**, 380 (2010).

[90] L. Sirovich, Turbulence and the dynamics of coherent structures. part i: Coherent structures, Quart. Appl. Math. **45**, 561 (1987).

[91] Z. Liu, R. J. Adrian, and T. J. Hanratty, Large-scale modes of turbulent channel flow: Transport and structure, J. Fluid Mech. **448**, 53 (2001).

[92] M. Placidi and B. Ganapathisubramani, Turbulent flow over large roughness elements: Effect of frontal and plan solidity on turbulence statistics and structure, Boundary-Layer Meteorol. **167**, 99 (2018).